Human-Inspired Active Compliant and Passive Shared Control Framework for Robotic Contact-Rich Tasks in Medical Applications

Junling Fu[†], *Student Member, IEEE*, Giorgia Maimone[†], Elisa Iovene, *Student Member, IEEE*, Jianzhuang Zhao, *Student Member, IEEE*, Alberto Redaelli, Giancarlo Ferrigno, *Senior Member, IEEE*, and Elena De Momi, *Senior Member, IEEE*

***Abstract*—This work presents a compliant and passive shared control framework for teleoperated robot-assisted tasks. Inspired by the human operator's capability of continuously regulating the arm impedance to perform contact-rich tasks, a novel control schema, exploiting the variable impedance control framework for force tracking is proposed. Moreover, bilateral teleoperation and shared control strategies are implemented to alleviate the human operator's workload. Furthermore, a global energy tank-based approach is integrated to enforce the system's passivity. The proposed framework is first evaluated to assess the force-tracking capability when the robot autonomously performs contact-rich tasks, e.g., in an ultrasound scanning scenario. Then, a validation experiment is conducted utilizing the proposed shared control framework. Finally, the system's usability is investigated with 12 users. The experiment results in system assessment revealed a maximum median error of 0.25 N across all the force-tracking experiment setups, i.e., constant and time-varying ones. Then, the validation experiment demonstrated significant improvements regarding the force tracking tasks compared to conventional control methods, and the system passivity was preserved during the task execution. Finally, the usability experiment shows that the human operator workload is significantly reduced by 54.6% compared to the other two control modalities. The proposed framework holds significant potential for the execution of remote robot-assisted medical procedures, such as palpation and ultrasound scanning, particularly in addressing deformation challenges while ensuring safety, compliance, and system passivity.**

***Index Terms*—Medical Robotics, Contact-Rich Tasks, Human-Robot Shared Control, Compliant Control, System Passivity;**

I. INTRODUCTION

ROBOTIC systems have been integrated into the medical domain, offering notable advantages over traditional manual task execution, including high precision capability, reduced trauma, improved ergonomics, and enhanced accessibility [1], [2]. Among the various control modalities, teleoperation remains the most conventional approach, allowing human operators to control the robot by transmitting and mapping human commands to the robot for task execution [3]. Nonetheless, the human operator typically needs to perform multiple tasks simultaneously, which requires significant hand-eye coordination capability and potentially imposes high physical and mental workloads. Consequently, increasing task completion performance while reducing the human operator's workload has gained more attention in recent years [4]. However, achieving fully autonomous systems remains a significant challenge, particularly given the typically unstructured, dynamic, and complicated medical scenarios [5]. Accordingly, the exploration of human-robot shared control frameworks has emerged as a promising paradigm, which leverages the human operator's decision-making and the controller's autonomous task execution capabilities [6], [7].

In medical applications, contact-rich tasks constitute a significant focus, encompassing palpation for diagnosis and abnormality detection [8], ultrasound for diagnosis and treatment [9], physical examination training [10], minimally invasive surgery operations [11], etc. Traditionally, manual-based modalities for medical contact-rich tasks entail clinicians or surgeons applying appropriate force and adjusting hand positions, or surgical instrument forces exerted on tissues or anatomical structures (e.g., controlling the pose and contact force of ultrasound probe) concurrently [12]. However, several challenges inherent in manual/traditional medical contact-rich tasks must be emphasized, including (i) a steep learning curve for novice clinicians to acquire expertise, leading to operator-dependent outcomes [13]; (ii) potential work-related musculoskeletal disorders caused by high physical workload [14]; and (iii) safety concerns such as infection risks due to clinician-patient contact [2]. Conversely, the integration of robotic systems to perform medical contact-rich tasks presents several advantages, including (i) standardized results, (ii) reduced workload during surgical task execution for the operator in the human-in-the-loop approach, and (iii) facilitating infection prevention by eliminating direct patient-surgeon contact.

Despite being deployed in medical robot applications to enhance precision and dexterity [3] (e.g., via motion scaling

---

This work was partially funded by the Progetti di Ricerca di Rilevante Interesse Nazionale (PRIN)-Bando 2022, under the project "FutuRO" (Grant Number: 2022342 MEF). Additionally, was partially funded by "THE - Tuscany Health Ecosystem" (ECS00000017, CUP I53C22000780001) as part of the NEXTGENERATIONEU program, specifically through Spoke 9, "Robotics and Automation for Health" for "REDIT" project (Robot-assisted Remote Echography for Diagnosis and Treatment).

Junling Fu, Giorgia Maimone, Elisa Iovene, Jianzhuang Zhao, Alberto Redaelli, Giancarlo Ferrigno, and Elena De Momi are with the Department of Electronics, Information, and Bioengineering (DEIB), Politecnico di Milano, 20133, Milan, Italy. (e-mail: junling.fu@polimi.it;giorgia.maimone@polimi.it; elisa.iovene@polimi.it;jianzhuang.zhao@polimi.it;alberto.redaelli@polimi.it; giancarlo.ferrigno@polimi.it;elena.demomi@polimi.it)

[†] These authors equally contributed to this work. *(Corresponding author: Junling Fu)*

for fine manipulation), provide remote access to expertise (e.g., rural areas), and mitigate infection risks, several inherent challenges in teleoperated robot-assisted contact-rich medical tasks still need to be addressed. Firstly, the modeling of the medical environment is challenging due to the nonlinear, deformable, anisotropic soft tissues and anatomical structures properties, alongside factors like friction force and elasticity [15], [16]. Additionally, the physical and cognitive workload imposed on human operators during the teleoperated task execution needs to be emphasized [17]. Furthermore, the safety and system stability (i.e., passivity) considering unforeseen disturbances, unstructured and dynamic environment, and human-robot-environment interaction should be clarified [18]. For instance, the explicit forces control strategy may exhibit instability in scenarios where contact is not fulfilled.

The remainder of this work is organized as follows. Section II describes the related works. Section III depicts the overall workflow and problem formulation. Section IV illustrates the details of the proposed control framework. Then, Section V gives the details of the system design and the experimental protocol. Section VI reports the experiment results. Finally, Section VII concludes this work.

II. RELATED WORKS

A. Control Strategies for Robotic Medical Contact-Rich Tasks

To address the safety concerns, force handling capabilities, and system stability in robot-assisted medical contact-rich scenarios, various solutions have been deployed. Specifically, according to the control strategies, they can be primarily classified into mechanism structure, model-based, optimization, and learning-based force control methods.

Mechanism's structure approaches are recognized for their cost-effectiveness, simplicity in control, and reliability. For instance, a novel force and position control mechanism was exploited for hand-held ultrasound tasks, which showcased the capability to mitigate instability issues induced by tissue deformation and human hand trembling [19]. Moreover, a constant-force mechanism was designed to facilitate stable force modulation in robot-assisted minimally invasive surgery tissue contact tasks [20]. However, customized mechanical design is inherently time-consuming and complex to achieve ideal force-tracking performance in contact-rich medical tasks.

General robotic manipulators have been extensively employed in performing medical contact-rich tasks. Conventionally, explicit control strategies have been deployed to track the desired force within simplistic control schemes. Nevertheless, the stability of such systems is susceptible to compromise, notably in the face of unforeseen external disturbance or sudden human movement, potentially resulting in pronounced oscillations [21]. Conversely, impedance control, which is an implicit control modality, has been employed to facilitate safe human-robot contact [22] [23]. However, accurate modeling of the tissue or anatomical structures and the environment was typically required when utilizing a constant impedance controller. For instance, a regression-based technique was employed to model the nonlinear tissue stiffness, which was further leveraged to correct the force-induced tissue deformation during the ultrasound imaging [24]. Nonetheless, the model-based approaches typically investigated the tool-tissue contact properties in a specific static position, thus the adaptation to the contact-rich tasks in a dynamic environment (e.g., sliding on tissue surface) remains a persistent challenge [11].

Alternatively, optimization and learning-based approaches have been exploited to address the force-tracking capability in robotic contact-rich tasks by finding the optimal parameters. For instance, in [25], a model predictive controller incorporating Hertz's contact theory was deployed to optimize both robot trajectories and regulate the contact force exerted on the deformable soft tissue. Subsequently, in [26], optimal impedance controller parameters to perform force-tracking in the contact-rich insertion scenario were solved by reformulating the problem as a Linear Quadratic Regulator (LQR). Additionally, Imitation Learning [27], Inverse Reinforcement Learning (IRL) [28], and Deep Learning (DL) [29] have been deployed to learn the optimal control law in performing robotic medical contact-rich tasks. However, the critical issues, including the reward function design, training process, and reliable simulation platform, should be further investigated.

B. Energy-based Robot System Passivity

Passivity-based control has emerged as a prevalent approach in achieving robust and stable interaction within unknown environments, serving as a sufficient condition for ensuring system stability [30] [31]. This control methodology has been seamlessly integrated into various robotic applications, including human-robot collaboration, robot-assisted rehabilitation, and bilateral teleoperation control [32], [33]. Within the context of energy and passivity theory, an *energy tank*-based approach has been exploited in robot control while preserving the passivity properties, ultimately fostering safe human-robot collaboration [34]. Notably, the *"tank"* was employed to store the energy dissipated by the system, which can subsequently be leveraged to replicate the desired behaviors (e.g., robot variable stiffness [35]). To ensure the system's passivity, a certain level of energy must always be preserved within the tank to execute the desired commands [35], [36].

Regarding the single robotic system passivity, the energy tank-based approach has been exploited to regulate the system passivity in robotic puncturing, accommodating variations in robot stiffness encountered during needle insertion and interaction with diverse anatomical structures (e.g., skin, kidney, and tumor) [35]. Moreover, in [37], a modulated tank-based strategy was utilized to facilitate optimal robot stability and task execution flexibility, which allows the robot to faithfully replicate desired behaviors while preserving robust stability across single-robot, multi-robot systems, and human-robot collaboration scenarios. Furthermore, an energy-based hierarchical passivity-enforced framework was exploited to regulate the time-varying robot stiffness, with predefined boundaries to constraint maximum allowable kinetic energy, thereby ensuring the energy injected into the robot system remains in a safe range during multiple priority contact task execution [38].

In contrast to systems employing a singular robot, bilateral or multilateral teleoperation control systems present heightened challenges, particularly in managing non-passive and unstable dynamics caused by factors such as haptic or force feedback, variable stiffness profiles, and latency issues. For instance, a two-layer-based approach, comprising the transparency layer and passivity layer, was deployed in a bilateral telemanipulation system to ensure stable behavior while accommodating unstable factors, including instances of hard contact, user grasp released, various stiffness profile, latency [39]. A novel single shared energy tank to interconnect multiple robots in a multi-master-multi-slave bilateral teleoperation system was proposed [40]. Specifically, each robot was endowed with controlled dissipation capabilities to harvest some energy to fill the shared tank when necessary. In [41], an energy tank aimed to ensure stable, time-varying interactive behaviors and seamless transitions between autonomous and bilateral teleoperation modes was developed in a teleoperated robotic surgery scenario. Compared to the individual local energy tanks, the global one was considered less conservative and yielded superior control performance in replicating the desired robotic behaviors [42], [43].

C. Human-Robot Shared Control for Medical Applications

Teleoperated robotic systems have garnered significant attention in the medical domain, considering their benefits, such as remote access capability, versatility, and adaptability. In [44], a novel scalable framework was deployed in a mimicked teleoperated robotic auscultation contact-rich task on a mock-up patient. Moreover, to mitigate the risk of secondary infection during the nasopharyngeal swab specimen collection, a teleoperated robotic system was developed for intuitive nasal sampling, which addresses remote center of motion and operability constraints concurrently [45]. Nevertheless, several critical issues inherent in teleoperated medical systems should be emphasized, including safety, reliability, operator comfort, and task completion performance.

Leveraging the human decision-making capabilities and the autonomy inherent in robot controllers, the shared control paradigm has emerged as a compelling paradigm in the robotics domain [46]. The shared control modality improved task completion performance while alleviating the human operator's cognitive workload [6]. A classification of shared control strategies for telerobotic systems has been investigated [47], and it mainly includes (i) the state guidance strategy and (ii) the semi-autonomous control strategy. For example, a novel shared control framework, exploiting the haptic guidance, was implemented to alleviate the human operator's workload with a 30% reduction in the perceived workload during the teleoperated manipulation task [48]. In the context of [42], a novel bilateral teleoperation architecture was crafted, leveraging the variable impedance controller to conduct robot-assisted contact tasks semi-autonomously. Specifically, the robot could dynamically adapt to the environment by modulating stiffness during task execution. Additionally, a shared control framework based on local autonomy was proposed to ensure transparency, fidelity, and robustness in teleoperated haptic-robot interaction. This technique employed a dual-proxy model to synchronize the two local autonomous controllers acting on the robot and the haptic device, thereby facilitating optimal motion and force reference based on the interaction tasks [49].

D. Contributions

This work introduces an active-compliant and passive human-robot shared control framework to address the aforementioned challenges in teleoperated robot-assisted medical contact tasks. The primary objective of the proposed framework is to enhance safe force-tracking capabilities in contact-rich scenarios via a compliant controller. Additionally, it aims to reduce the physical and cognitive workload of human operators during the execution of teleoperated contact-rich tasks and maintain system passivity throughout task execution.

Specifically, the proposed framework integrates Quadratic Programming (QP)-based online optimization, variable impedance control, and human-robot shared control while ensuring system passivity through global energy-based enforcement mechanisms. The primary contributions of this study can be summarized as follows:

- (i) An active compliant control strategy that leverages the QP optimization and variable impedance controller is proposed to ensure safety and for desired force regulation during robot-assisted contact-rich tasks.
- (ii) A global energy tank is introduced to preserve the whole system's passivity during the task execution.
- (iii) A human-robot shared control strategy is implemented to mitigate human operators' physical and cognitive demands during contact-rich task execution.

Finally, comprehensive validation experiments have been conducted on a simplified mock-up medical scenario to evaluate the effectiveness of the proposed framework.

III. ARCHITECTURE AND PROBLEM FORMULATION

A. Overall View of Proposed Framework

Fig.1 illustrates the architecture of the proposed framework, the primary modules and functionalities are listed below.

- *Operator and Haptic Interface:* The haptic device enables human operators to transmit commands by capturing hand movements, denoted as $\dot{\boldsymbol{x}}_{\boldsymbol{m}}$. Additionally, a monitor provides real-time visual feedback to the operator during task execution, facilitating better situational awareness.
- *Bilateral Teleoperation Control:* Commands generated by the human operator are recorded and appropriately scaled before being transmitted to the follower robot for execution. Concurrently, haptic feedback forces, $\boldsymbol{F}_{\boldsymbol{f}}^{\boldsymbol{m}}$, are sent back to the operator, establishing bilateral teleoperation.
- *Compliant Controller*: A Cartesian Impedance Controller is employed to execute contact-rich tasks, which ensures compliance and promotes safety during interactions between the robot and the medical environment.
- *QP-Optimization:* QP optimization is exploited to calculate the optimal robot stiffness, $\boldsymbol{K}_{\boldsymbol{opt}}$, for the Cartesian Impedance controller, which is essential for ensuring efficient and effective execution of contact-rich tasks, particularly on force tracking.

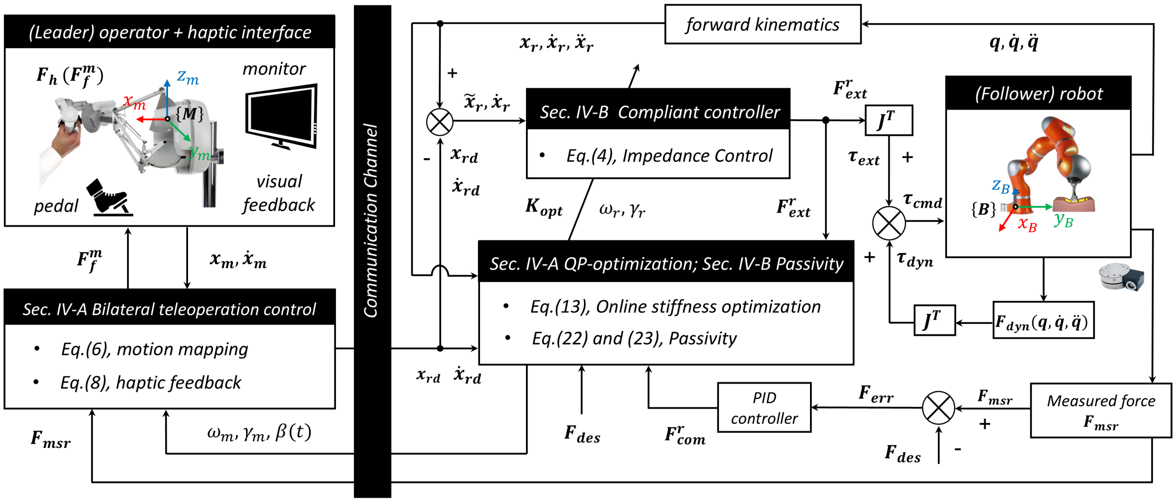

Fig. 1. Block diagram of the proposed control framework. The left and right panels represent the local leader and remote follower sides, respectively. Specifically, the human operator applies the force, $\boldsymbol{F_h}$ on the haptic interface. The input movement, $\dot{\boldsymbol{x}}_{\boldsymbol{m}}$, is then scaled, and the desired robot position, $\boldsymbol{x_{r_d}}$, is sent to the robot afterward; $\aleph$ and η are the parameters to enable and disable the teleoperation control and motion scaling. $\boldsymbol{F_f^m}$ is the haptic feedback force. ω_m, γ_m, and $\beta(t)$ are the parameters to modify the controller and ensure system passivity. $\boldsymbol{K_{opt}}$ is the optimal stiffness of the Cartesian Impedance controller. $\boldsymbol{Q}$ and $\boldsymbol{R}$ are the weighting parameters in the optimization function. $\boldsymbol{F_{msr}}$ is measured by the external force/torque sensor to formulate the closed-loop force control by integrating the error compensation term, $\boldsymbol{F^r_{com}}$, calculated by the PID controller. The desired contact force, $\boldsymbol{F_{des}}$, is initialized as input based on the scenario. The robot joint states $(\boldsymbol{q}, \dot{\boldsymbol{q}}, \ddot{\boldsymbol{q}})$ are acquired, $\boldsymbol{x_r}, \dot{\boldsymbol{x}}_{\boldsymbol{r}}, \ddot{\boldsymbol{x}}_{\boldsymbol{r}} \in \mathbb{R}^m$ are the measured position, velocity, and acceleration terms in Cartesian space derived from the forward kinematics. $\boldsymbol{J}^T$ is the transpose of the Jacobin matrix. The dynamics of the robotic manipulator $\boldsymbol{F_{dyn}}(\boldsymbol{q}, \dot{\boldsymbol{q}}, \ddot{\boldsymbol{q}})$ is compensated.

- *System Passivity:* A passivity module ensures the overall passivity of the system. This is achieved by leveraging energy tank-based enforcement and dynamically adjusting the parameters of both the bilateral teleoperation control and the compliant controller.

The connection between the *"leader"* (human operator, illustrated in the left panel) and the *"follower"* (robot, depicted in the right panel) components in Fig.1 is established via an Ethernet cable, which serves as the communication channel (labeled as the *"communication channel"* in Fig.1). Notably, the delays in the communication channel are not considered in the proposed framework. On the *"leader"* side, a haptic device operates on a desktop computer connected via a USB protocol, with a pedal used to activate and deactivate the *"bilateral teleoperation control"*. On the *"follower"* side, the real-time computation of *"QP-optimization"* and *"system passivity"* is executed on the desktop computer. Subsequently, the generated commands and haptic feedback forces are transmitted to the *"compliant controller"* and *"bilateral teleoperation control"* modules to facilitate task execution. The system's data exchange relies on the Robot Operating System (ROS) communication protocol. Further details about the device implementation are provided in Section V-A.

B. Dynamics of the Robot and Compliant Control

1) Dynamics of the Robotic Manipulator: Without loss of generality, the dynamics of a n-DoFs serial robotic manipulator in the m-DoFs Cartesian space is formulated as:

$$\boldsymbol{M_r}(\boldsymbol{x_r})\ddot{\boldsymbol{x}}_{\boldsymbol{r}} + \boldsymbol{C_r}(\boldsymbol{x_r}, \dot{\boldsymbol{x}}_{\boldsymbol{r}})\dot{\boldsymbol{x}}_{\boldsymbol{r}} + (\boldsymbol{J}^\dagger)^T \boldsymbol{G_r}(q) - \boldsymbol{F^r_{ext}} = \boldsymbol{F^r_{cmd}} \quad (1)$$

where $\boldsymbol{M_r}, \boldsymbol{C_r} \in \mathbb{R}^{m\times m}$, and $\boldsymbol{G_r} \in \mathbb{R}^m$ represents the symmetric and positive definite mass matrix, the Coriolis and Centrifugal matrix, and the gravitational vector, respectively. $\boldsymbol{x_r}, \dot{\boldsymbol{x}}_{\boldsymbol{r}}, \ddot{\boldsymbol{x}}_{\boldsymbol{r}} \in \mathbb{R}^m$ are the measured position, velocity, and acceleration terms in Cartesian space; $\boldsymbol{q}, \dot{\boldsymbol{q}} \in \mathbb{R}^n$ are the vectors of the joint angles and velocities. $\boldsymbol{\tau_{ext}} \in \mathbb{R}^n$ and $\boldsymbol{\tau_{cmd}} \in \mathbb{R}^n$ are the vectors of external and command torques to the robot. Specifically, $\boldsymbol{F^r_{ext}}, \boldsymbol{F^r_g}, \boldsymbol{F^r_{cmd}} \in \mathbb{R}^m$ are the external, gravity, and commanded force of the robotic manipulator and calculated by: $\boldsymbol{\tau_{ext}} = \boldsymbol{J}(\boldsymbol{q})^T \boldsymbol{F^r_{ext}}$, $\boldsymbol{G}(\boldsymbol{q}) = \boldsymbol{J}(\boldsymbol{q})^T \boldsymbol{F^r_g}(\boldsymbol{x})$, $\boldsymbol{\tau_{cmd}} = \boldsymbol{J}(\boldsymbol{q})^T \boldsymbol{F^r_{cmd}}$, respectively. $\boldsymbol{J}(\boldsymbol{q}) \in \mathbb{R}^{m\times n}$ is the Jacobian matrix of the robotic manipulator. $\boldsymbol{J}^\dagger$ represents the generalized inverse of the Jacobian matrix and can be computed using the right-hand Moore-Penrose pseudo-inverse. Furthermore, $\boldsymbol{M_r}(\boldsymbol{x_r})$ and $\boldsymbol{C_r}(\boldsymbol{x_r}, \dot{\boldsymbol{x}}_{\boldsymbol{r}})$ are approximately calculated by [50]:

$$\boldsymbol{M_r}(\boldsymbol{x_r}) = \left(\boldsymbol{J}\boldsymbol{M_r}(\boldsymbol{q})^{-1}\boldsymbol{J}^T\right)^{-1} \quad (2)$$

$$\boldsymbol{C_r}(\boldsymbol{x_r}, \dot{\boldsymbol{x}}_{\boldsymbol{r}}) = (\boldsymbol{J}^\dagger)^T \left[\boldsymbol{C_r}(\boldsymbol{q}, \dot{\boldsymbol{q}}) - \boldsymbol{M_r}(\boldsymbol{q})\boldsymbol{J}^\dagger \dot{\boldsymbol{J}}\right] \boldsymbol{J}^\dagger \quad (3)$$

2) Compliant controller: To facilitate safe contact between the robot and the target anatomical structure during the contact-rich task, a compliant controller is exploited, as presented in Eq.(4), which is represented by the *Mass-Spring-Damper* (*MSD*) system. The external contact force of the robot, $\boldsymbol{F^r_{ext}} \in \mathbb{R}^m$, can be approximately calculated by [51]:

$$\boldsymbol{F^r_{ext}} = \boldsymbol{M_c}\ddot{\boldsymbol{x}}_{\boldsymbol{r}} - \boldsymbol{D_c}\dot{\boldsymbol{x}}_{\boldsymbol{r}} + \boldsymbol{K_c}\tilde{\boldsymbol{x}}_{\boldsymbol{r}} \quad (4)$$

where $\tilde{\boldsymbol{x}}_{\boldsymbol{r}}$, $\dot{\boldsymbol{x}}_{\boldsymbol{r}}$, and $\ddot{\boldsymbol{x}}_{\boldsymbol{r}} \in \mathbb{R}^m$ are the robot end effector position displacement between the measured and commanded one, velocity, and acceleration in the Cartesian space. $\tilde{\boldsymbol{x}}_{\boldsymbol{r}}$ is calculated as $\tilde{\boldsymbol{x}}_{\boldsymbol{r}} = \boldsymbol{x_{rd}} - \boldsymbol{x_r}$, where $\boldsymbol{x_{rd}}$ and $\boldsymbol{x_r} \in \mathbb{R}^m$ are the desired and current robot end effector position. $\boldsymbol{M_c}$, $\boldsymbol{K_c}$ and, $\boldsymbol{D_c} \in \mathbb{R}^{m\times m}$ denote the positive definite mass, stiffness, and damping parameters of the robot controller. $\boldsymbol{D_c}$ can be calculated by the damping law $\boldsymbol{D_c} = 2\xi\sqrt{\boldsymbol{M_c K_c}}$, where ξ is the positive damping coefficient and $\xi = 1$ represents the coefficient for critical damping. Moreover, Eq. (4) can be simplified into a *Spring-Damper* model by neglecting the $\boldsymbol{M_c \ddot{x}_r}$ term in scenarios involving low-speed motion.

C. Bilateral Teleoperation Control

1) Dynamics of Haptic Device: Similarly, assuming that the gravity force is pre-compensated, the dynamics of a m-DoFs haptic device in the Cartesian space is given by:

$$\boldsymbol{M_m}(\boldsymbol{x_m})\boldsymbol{\ddot{x}_m} + \boldsymbol{C_m}(\boldsymbol{x_m}, \boldsymbol{\dot{x}_m})\boldsymbol{\dot{x}_m} - \boldsymbol{F_f^m} = \boldsymbol{F_{cmd}^m} \tag{5}$$

where $\boldsymbol{M_m}, \boldsymbol{C_m} \in \mathbb{R}^{m\times m}$ are the symmetric and positive definite Mass matrix and the Coriolis and Centrifugal matrix, respectively. $\boldsymbol{F_f^m}$ and $\boldsymbol{F_{cmd}^m} \in \mathbb{R}^m$ are the external and commanded forces of the haptic interface. Furthermore, $\boldsymbol{x_m}$ and $\boldsymbol{\dot{x}_m}, \boldsymbol{\ddot{x}_m} \in \mathbb{R}^m$ are the measured position, velocity, and acceleration terms of the leader side haptic device.

2) Teleoperation control: As illustrated in Fig.1, an incremental teleoperation control method is adopted to enlarge the workspace of the leader by switching the system state using the pedal of the haptic device. Specifically, the teleoperation control is activated when the human operator steps on the pedal. The human hand movement can be sent to the robot on the remote side and vice versa. Consequently, the remote side robot position can be expressed as below:

$$\boldsymbol{x_{rd}}(t) = \boldsymbol{x_{rd}}(t_0) + \aleph \int_{t_o}^{t_s} \eta\, {}^{r}_{m}T \boldsymbol{\dot{x}_m}\, dt \tag{6}$$

where t_0 and t_s are the time instant of the pedal switch on and off; $\boldsymbol{x_{rd}}(t_0) \in \mathbb{R}^m$ and $\boldsymbol{x_{rd}}(t) \in \mathbb{R}^m$ are the robot's initial and desired positions during the task execution; $\aleph$ is the parameter used to enable and disable the teleoperation control via the state switch pedal of the haptic device, which is expressed as:

$$\aleph = \begin{cases} 0, & \textit{pedal off} \\ 1, & \textit{pedal on} \end{cases} \tag{7}$$

where η is a positive motion scaling parameter, which can be specified according to the task; ${}^{r}_{m}T \in \mathbb{R}^{m\times m}$ is the transformation matrix from the haptic device $\{\boldsymbol{M}\}$ to the robot $\{\boldsymbol{B}\}$ frame, which is determined by the relative position between the robot and the haptic device. $\boldsymbol{\dot{x}_m} \in \mathbb{R}^m$ is the measured velocity of the leader side haptic device in the Cartesian space.

3) Haptic feedback: To improve the human operator's situational awareness during the task execution, the feedback force $\boldsymbol{F_f^m} \in \mathbb{R}^m$ is provided to the human operator via the haptic device, which is expressed as

$$\boldsymbol{F_f^m} = -\beta(t)\boldsymbol{F_{msr}^r} - \boldsymbol{D_m}\boldsymbol{\dot{x}_m} \tag{8}$$

$\boldsymbol{D}_m \in \mathbb{R}^{m\times m}$ is a damping coefficient to stabilize the teleoperation; $\beta(t)$ is a variable used for the gradual occurrence of the force feedback to avoid oscillation and calculated by:

$$\beta(t) = \frac{1}{2}\left(1 - \cos\left(\frac{\pi(t - t_s)}{t_f - t_s}\right)\right), t_s < t < t_f \tag{9}$$

t_s and t_f represent the starting and finishing time for smooth, haptic force feedback. Specifically, the function is designed to vary gradually from 0 to 1, aligning with the start and end of the force feedback smoothing time window.

D. Problem Formulation

1) Compliant force control: Typically, in scenarios involving rigid contacts, the deformation of the material caused by the contact is minor, and almost equal to zero. However, in soft material contact scenarios, the deformation is significant, and the force calculated by the MSD model could not represent the actual contact force when in contact with deformable objects [11]. When exploiting a constant stiffness value in Eq.(4), $\boldsymbol{\tilde{x}_r}$ needs to be experimentally explored [52] to achieve acceptable desired force tracking performance. Alternatively, instead of setting an appropriate $\boldsymbol{\tilde{x}_r}$ and leveraging a constant stiffness coefficient, an optimization-based solution can be formulated by actively finding the optimal time-varying robot stiffness, $\boldsymbol{K_{opt}}$, to track the desired contact force, $\boldsymbol{F_{des}}$.

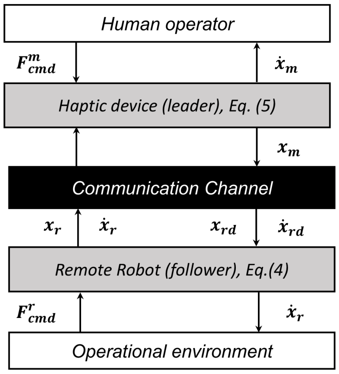

Fig. 2. Characterization of the communication block in a bilateral teleoperation control framework [53].

2) System passivity analysis: The calculated optimal robot stiffness profile, $\boldsymbol{K_{opt}}(t)$, is time-varying, and the passivity of the system could be violated. Specifically, taking into consideration the power ports $\left(\boldsymbol{\dot{x}_r}, \boldsymbol{F_{cmd}^r}\right)$ from the remote robot side and $\left(\boldsymbol{\dot{x}_m}, \boldsymbol{F_{cmd}^m}\right)$ from the leader haptic device side in a bilateral teleoperation control framework [53], as depicted in Fig.2. $\boldsymbol{\dot{x}_m} \in \mathbb{R}^m$ is the measured velocity of the leader side haptic device in the Cartesian space and $\boldsymbol{F_f^m} \in \mathbb{R}^m$ is the external force applied on the haptic interface. According to the passivity definition, the system passivity can be guaranteed when the following condition is fulfilled:

$$V(t) - V(t_0) \leq \int_0^t \left(\boldsymbol{\dot{x}_r^T F_{cmd}^r} + \boldsymbol{\dot{x}_m^T F_{cmd}^m}\right) dt \tag{10}$$

where V is the energy storage function, $V(t)$ and $V(t_0)$ denotes the stored energy at time t and t_0, respectively.

The energy of the developed bilateral teleoperation control system, $V(t)$, is composed of the kinetic energy, V_k, and elastic potential energy, V_e, which is formulated as below:

$$V = \underbrace{\frac{1}{2}\boldsymbol{\dot{x}_m^T M_m \dot{x}_m} + \frac{1}{2}\boldsymbol{\dot{x}_r^T M_r \dot{x}_r}}_{V_k} + \underbrace{\frac{1}{2}\boldsymbol{\tilde{x}_r^T K_c \tilde{x}_r}}_{V_e} \tag{11}$$

where $\boldsymbol{M_r} \in \mathbb{R}^{m\times m}$ represents the symmetric and positive definite mass matrix. Furthermore, taking the time derivative of the energy equation, V, in Eq. (11) and substituting the

$\ddot{\boldsymbol{x}}_{\boldsymbol{m}}, \ddot{\boldsymbol{x}}_{\boldsymbol{r}}$ terms obtained from Eq. (1) and Eq. (5), and leveraging the property that the Mass, Coriolis, and Centrifugal matrix $\left[\dot{\boldsymbol{M}}(\boldsymbol{x}) - 2\boldsymbol{C}(\boldsymbol{x}, \dot{\boldsymbol{x}})\right]$ is a skew-symmetric one [35], the following formulation can be obtained:

$$\dot{V} = \underbrace{\dot{\boldsymbol{x}}_{\boldsymbol{r}}^{T} \boldsymbol{F}^{\boldsymbol{r}}_{\boldsymbol{cmd}} - \dot{\boldsymbol{x}}_{\boldsymbol{r}}^{T} \boldsymbol{D}_{\boldsymbol{c}} \dot{\boldsymbol{x}}_{\boldsymbol{r}} + \dot{\boldsymbol{x}}_{\boldsymbol{m}}^{T} \boldsymbol{F}^{\boldsymbol{m}}_{\boldsymbol{cmd}} - \dot{\boldsymbol{x}}_{\boldsymbol{m}}^{T} \boldsymbol{D}_{\boldsymbol{m}} \dot{\boldsymbol{x}}_{\boldsymbol{m}}}_{passive} + \underbrace{\left[\frac{1}{2}\tilde{\boldsymbol{x}}_{\boldsymbol{r}}^{T} \dot{\boldsymbol{K}}_{\boldsymbol{c}} \tilde{\boldsymbol{x}}_{\boldsymbol{r}} + \dot{\boldsymbol{x}}_{\boldsymbol{rd}}^{T} \boldsymbol{K}_{\boldsymbol{c}} \tilde{\boldsymbol{x}}_{\boldsymbol{r}} - \dot{\boldsymbol{x}}_{\boldsymbol{m}}^{T} \boldsymbol{F}^{\boldsymbol{r}}_{\boldsymbol{msr}}\right]}_{uncertain} \tag{12}$$

The derivation process for Eq. (12) is comprehensively detailed in the Appendix. Specifically, as shown in Eq. (12), the sign of the squared brackets is uncertain, i.e., can be positive or negative, and the passivity condition expressed in Eq. (10) could not be guaranteed.

Safety and stability concerns: To ensure safe interaction during contact-rich tasks and enforcing system passivity, this study focuses on two key aspects, outlined as follows:

- In this work, a novel QP-based optimization strategy is proposed, as described later in Section IV-A.
- To preserve the system's passivity of the proposed framework, a global energy tank-based approach is developed, as presented later in Section IV-B.

IV. PROPOSED CONTROL FRAMEWORK

A. Active Compliant Control for Medical Contact-Rich Task

1) Multiple tasks optimization: Although the Impedance Controller allows the robot to perform contact-rich tasks in a compliant manner, the balance between the task completion performance (i.e., the force tracking task) and compliance should be considered. To facilitate steady and effective execution of the contact-rich task within the medical context, the robotic system is expected to have a trade-off between force tracking and compliance behavior with different levels of priorities. For instance, executing the force-tracking tasks while maintaining the robot's compliance simultaneously.

To achieve this, a novel online optimization strategy is introduced in the contact-rich scenarios, which simultaneously considers both (i) the force-tracking capability and (ii) the robot environment-compliant contact behavior. Specifically, this is achieved through a dual optimization framework, which is expressed below:

$$\min_{\boldsymbol{K}_{\boldsymbol{c}} \in \mathbb{R}^{m \times m}} \underbrace{\frac{1}{2}\sum_{n=1}^{N} \left\| {\boldsymbol{F}^{\boldsymbol{r}}_{\boldsymbol{ext}}}^{n} - \left(\boldsymbol{F}_{\boldsymbol{des}} + \boldsymbol{F}^{\boldsymbol{r}}_{\boldsymbol{com}}\right) \right\|^{2}_{\boldsymbol{Q}}}_{force\ tracking} + \underbrace{\frac{1}{2}\sum_{n=1}^{N} \left\| {\boldsymbol{K}_{\boldsymbol{opt}}}^{n} - \boldsymbol{K}_{\boldsymbol{min}} \right\|^{2}_{\boldsymbol{R}}}_{compliance} \tag{13}$$

where $\boldsymbol{K}_{\boldsymbol{opt}}(t) \in \mathbb{R}^{m}$ is the optimized stiffness at time instant t. n represents the length of time frames considered in the optimization problem (In this work, $n = 1$ has been leveraged for real-time optimization). $\|\cdot\|^2$ represents the two-norm calculation. $\boldsymbol{Q}$ and $\boldsymbol{R} \in \mathbb{R}^{m \times m}$ are the diagonal positive definite weighting matrices. Specifically, a high value of $\boldsymbol{Q}$ means the primary priority for force tracking, while the robot compliance can be adjusted by setting a proper $\boldsymbol{R}$ value. $\boldsymbol{K}_{\boldsymbol{min}}$ represents the minimum robot stiffness value during the task execution. $\boldsymbol{F}^{\boldsymbol{r}}_{\boldsymbol{com}}$ is the compensated force error term that is integrated into Eq.(13) to formulate closed-loop force tracking control.

Furthermore, inspired by the human operator's capability of instinctively reducing their effort or arm stiffness to prevent damage to the environment (i.e., delicate objects), several similar constraints have been incorporated into the optimization problem. Specifically, the constraints should be imposed considering the hardware limitations and safety, including:

- (i) the robot stiffness profile, $\boldsymbol{K}_{\boldsymbol{c}}$, needs to be regulated to avoid damaging the robotic manipulator and ensure the system compliance, which is denoted as $\boldsymbol{K}_{\boldsymbol{min}} \leq \boldsymbol{K}_{\boldsymbol{c}} \leq \boldsymbol{K}_{\boldsymbol{max}}$. Where $\boldsymbol{K}_{\boldsymbol{min}}$ and $\boldsymbol{K}_{\boldsymbol{max}}$ are set appropriately based on specified scenarios.
- (ii) the maximum allowed contact force, $\boldsymbol{F}_{\boldsymbol{max}}$, should be regulated to avoid damaging the anatomical structures, which is expressed by: $0 \leq \left\|\boldsymbol{F}^{\boldsymbol{r}}_{\boldsymbol{ext}}\right\| \leq \boldsymbol{F}_{\boldsymbol{max}}$.

2) Closed-loop force tracking: Considering the nonlinear properties and non-uniformity of deformable materials [25], e.g., soft tissue, the approximate force $\boldsymbol{F}^{\boldsymbol{r}}_{\boldsymbol{ext}}$, calculated by the *Mass-Spring-Damper* model in Eq. (4), could not represent the actual contact force in deformable contact-rich scenarios [11], [54]. Consequently, to track the desired contact force, $\boldsymbol{F}_{\boldsymbol{des}}$, a proportional–integral–derivative controller (PID) control scheme is utilized to calculate the compensated force term, $\boldsymbol{F}^{\boldsymbol{r}}_{\boldsymbol{com}}(t)$ at the time instant t, and integrated into the optimization formula, which is expressed as below:

$$\boldsymbol{F}^{\boldsymbol{r}}_{\boldsymbol{com}}(t) = \boldsymbol{K}_{\boldsymbol{p}} \boldsymbol{F}_{\boldsymbol{err}}(t) + \boldsymbol{K}_{\boldsymbol{i}} \int_{t_s}^{t_e} \boldsymbol{F}_{\boldsymbol{err}}(t)dt + \boldsymbol{K}_{\boldsymbol{d}} \frac{d\boldsymbol{F}_{\boldsymbol{err}}(t)}{dt} \tag{14}$$

where $\boldsymbol{F}_{\boldsymbol{err}} \in \mathbb{R}^{m}$ is the force-tracking error and calculated by:

$$\boldsymbol{F}_{\boldsymbol{err}} = \boldsymbol{F}_{\boldsymbol{des}} - \boldsymbol{F}_{\boldsymbol{msr}} \tag{15}$$

where $\boldsymbol{F}_{\boldsymbol{des}}$ and $\boldsymbol{F}_{\boldsymbol{msr}} \in \mathbb{R}^{m}$ are the desired and measured contact forces during the task. $\boldsymbol{K}_{\boldsymbol{p}}$, $\boldsymbol{K}_{\boldsymbol{i}}$, and $\boldsymbol{K}_{\boldsymbol{d}} \in \mathbb{R}^{m}$ are the proportional, integral, and derivative gains of the PID controller, respectively. t_s, t_e, and Δt represent the starting and ending time sliding windows considered in the integration and the discrete-time of the control loop, respectively.

3) QP optimization formulation: In this work, $\boldsymbol{K}_{\boldsymbol{opt}}(t)$ is estimated in real-time to track the desired contact force. Moreover, considering the typically low-speed requirement in medical applications, (e.g., 5-20 mm/s is adopted in ultrasound imaging scenario), Eq. (4) can be further simplified as a *Spring-Damper* model by neglecting the $\boldsymbol{M}_{\boldsymbol{c}} \ddot{\boldsymbol{x}}_{\boldsymbol{r}}$ term. Subsequently, by substituting the force $\boldsymbol{F}^{\boldsymbol{r}}_{\boldsymbol{ext}}$, calculated by Eq. (4) into the Eq. (13), an objective function, $f\left(\boldsymbol{K}_{\boldsymbol{opt}}\right)$, can be defined and formulated as:

$$\begin{aligned} f\left(\boldsymbol{K}_{\boldsymbol{opt}}\right) = & \frac{1}{2}\boldsymbol{K}_{\boldsymbol{opt}}^{T} [\tilde{\boldsymbol{x}}_{\boldsymbol{r}}^{T} \boldsymbol{Q} \tilde{\boldsymbol{x}}_{\boldsymbol{r}} + \boldsymbol{R}] \boldsymbol{K}_{\boldsymbol{opt}} \\ & + [\boldsymbol{Q} \tilde{\boldsymbol{x}}_{\boldsymbol{r}} (\boldsymbol{D}_{\boldsymbol{c}} \dot{\boldsymbol{x}}_{\boldsymbol{r}} - (\boldsymbol{F}_{\boldsymbol{des}} + \boldsymbol{F}^{\boldsymbol{r}}_{\boldsymbol{com}})) - \boldsymbol{R} \boldsymbol{K}_{\boldsymbol{min}}] \boldsymbol{K}_{\boldsymbol{opt}} \end{aligned} \tag{16}$$

To minimize the objective function $f\left(\boldsymbol{K_{opt}}\right)$, Eq.(16) can be further formulated as the general expression of QP, which is expressed as below:

$$\min_{\boldsymbol{x}\in\mathbb{R}^m} f(\boldsymbol{x}) = \frac{1}{2}\boldsymbol{x}^T\boldsymbol{G}\boldsymbol{x} + \boldsymbol{b}^T\boldsymbol{x} \tag{17}$$

where $\boldsymbol{x} \in \mathbb{R}^m$ and $\boldsymbol{b} \in \mathbb{R}^m$ are vectors, $\boldsymbol{G} \in \mathbb{R}^{m\times m}$ is the symmetric matrix.

Furthermore, to formulate the proposed optimization problem in Eq. (16) as the general expression in Eq. (17) and ensure all the matrices follow the criteria for a standard QP problem, the following formulation is implemented:

$$\boldsymbol{G} = \boldsymbol{\tilde{x}_r^T Q \tilde{x}_r} + \boldsymbol{R} \tag{18}$$

$$\boldsymbol{b} = [\boldsymbol{Q\tilde{x}_r}(\boldsymbol{D_c\dot{x}_r} - (\boldsymbol{F_{des}} + \boldsymbol{F^r_{com}})) - \boldsymbol{RK_{min}}] \tag{19}$$

where $\boldsymbol{G}$ and $\boldsymbol{b}$ are the quadratic and linear items in the standardized QP optimization function. Then, the optimal robot stiffness, $\boldsymbol{K_{opt}}(t)$ for performing the medical contact-rich task can be obtained.

This section introduces an active compliant control strategy to enhance safety and improve force-tracking performance. Unlike traditional approaches that rely on explicit force control or a constant Cartesian Impedance Controller, the proposed strategy integrates QP optimization for real-time adjustment of robot stiffness and incorporates closed-loop force control.

B. Global Energy Tank-Enhanced System Passivity

1) Energy tank formulation: To tackle the above-mentioned system passivity issue in Section III-D2, a promising solution is to design a passivity-preserving control strategy to regulate the system behavior, e.g., robot stiffness, $\boldsymbol{K_c}$, and haptic feedback force, $\boldsymbol{F^m_f}$. Therefore, an energy tank-based control strategy is utilized to enforce the proposed framework passivity, the details are summarized in Algorithm.1.

The energy stored in the tank, $T(s_t)$ is defined as a function of the tank state as below:

$$T(s_t) = \frac{1}{2}{s_t}^2 \tag{20}$$

where $s_t \in \mathbb{R}$ is the tank state at the time instant t.

Remark 1: When the intended robotic behavior requires more than passive engagement and there is limited energy available, incorporating a damper term into the system presents a promising solution that allows the system to harvest energy, and refill the energy tank while maintaining passivity [37], [42]. Consequently, the robotic system can effectively execute the desired behavior without compromising its passive nature.

Afterwards, considering the power ports for energy exchange between the system and the environment, i.e., $\left(\boldsymbol{\dot{x}_r}, \boldsymbol{F^r_{cmd}}\right)$ from the robot side and $\left(\boldsymbol{\dot{x}_m}, \boldsymbol{F^m_{cmd}}\right)$ from the leader side, the tank dynamics can be formulated as [42]:

$$\begin{aligned}\dot{s}_t =& \frac{\sigma_m \boldsymbol{\dot{x}_m^T D_m \dot{x}_m}}{s_t} + \frac{\sigma_r \boldsymbol{\dot{x}_r^T D_c \dot{x}_r}}{s_t} + \frac{\omega_m \boldsymbol{\dot{x}_m^T F^r_{msr}}}{s_t} \\ &- \frac{\omega_r \boldsymbol{\dot{x}_r^T K_c \tilde{x}_r}}{s_t} + \underbrace{\frac{\gamma_m \boldsymbol{\dot{x}_m^T D_{m,h} \dot{x}_m}}{s_t} + \frac{\gamma_r \boldsymbol{\dot{x}_r^T D_{r,h} \dot{x}_r}}{s_t}}_{\textit{damping injection}}\end{aligned} \tag{21}$$

Algorithm 1 Energy Tank-Based System Passivity

Initialization: Initialize the energy stored in the tank with $T(s_0) = E_0 = \underline{E}$

```
while Shared-control loop is active do
    if $T(s_t) \le \underline{E}$ then
        $\sigma_m = 1, \quad \sigma_r = 1$
        $\omega_m = 0, \quad \omega_r = 0$
        $\gamma_m = 1, \quad \gamma_r = 1$
    else if $\underline{E} < T(s_t) < \bar{E}$ then
        $\sigma_m = 1, \quad \sigma_r = 1$
        $\omega_m = 1, \quad \omega_r = 1$
        $\gamma_m, \gamma_r = \frac{1}{2}\left(1 + \cos\left(\frac{\pi(E-\underline{E})}{\bar{E}-\underline{E}}\right)\right)$    ▷ Eq. (25)
    else if $T(s_t) \ge \bar{E}$ then
        $\sigma_m = 0, \quad \sigma_r = 0$
        $\omega_m = 1, \quad \omega_r = 1$
        $\gamma_m = 0, \quad \gamma_r = 0$
    end if
    Update the energy tank state $\dot{T}(s_t)$ using Eq. (24)
    $T(s_t) = T(s_{t-1}) + \dot{T}(s_t)\Delta t$    ▷ Discrete model
end while
```

where σ_m and σ_r are the parameters that manage the amount of energy stored in the tank through the dissipation channel (inject energy to the tank), which is expressed as:

$$\sigma_m, \sigma_r = \begin{cases} 1, & \textit{if } T(s_t) < \bar{E}, \\ 0, & \textit{otherwise} \end{cases} \tag{22}$$

where $\bar{E}$ represents the upper boundary of energy that can be stored in the tank for implementing the non-passive practical application.

Similarly, a minimum amount of energy, $\underline{E}$, must always be kept in the tank to avoid singularity. ω_m and ω_r are adopted to modify the control actions when the energy level in the tank reaches the lower limit $\underline{E}$, which are expressed below:

$$\omega_m, \omega_r = \begin{cases} 1, & \textit{if } T(s_t) > \underline{E}, \\ 0, & \textit{otherwise} \end{cases} \tag{23}$$

The rate of the energy change in the tank, $\dot{T}(s_t)$, can be obtained by its derivation and expressed as below:

$$\begin{aligned}\dot{T}(s_t) =& \dot{s}_t s_t = \sigma_m \boldsymbol{\dot{x}_m^T D_m \dot{x}_m} + \sigma_r \boldsymbol{\dot{x}_r^T D_c \dot{x}_r} + \omega_m \boldsymbol{\dot{x}_m^T F^r_{msr}} \\ &- \omega_r \boldsymbol{\dot{x}_r^T K_c \tilde{x}_r} + \gamma_m \boldsymbol{\dot{x}_m^T D_{m,h} \dot{x}_m} + \gamma_r \boldsymbol{\dot{x}_r^T D_{r,h} \dot{x}_r}\end{aligned} \tag{24}$$

where σ_m and σ_r are the parameters that manage the amount of energy stored in the tank through the dissipation channel (inject energy to the tank); ω_m and ω_r are the parameters that are utilized to modify the control actions. γ_m and γ_r are the coefficients that allow the additional damping term $\boldsymbol{D_{m,h}}$ and $\boldsymbol{D_{r,h}}$ to be injected into the system [42].

Specifically, the *damping injection* parameters γ_m and γ_r in this work are designed to smoothly rise from 0 to 1 according to the current amount of energy, E, reserved in the tank. Specifically, γ_m and γ_r are calculated as below:

$$\gamma_m, \gamma_r = \frac{1}{2}\left(1 + \cos\left(\frac{\pi(E - \underline{E})}{\bar{E} - \underline{E}}\right)\right) \tag{25}$$

where $\underline{E}$ and $\bar{E}$ are the lower and upper boundaries of energy stored in the tank. Furthermore, considering integration of the system passivity regulation, the original haptic feedback force, $\boldsymbol{F_f^m}$ in Eq. (8) and the robot Cartesian impedance controllers represented by Eq. (4) can be reformulated as follows:

$$\begin{cases} \boldsymbol{F_f^m} = -\omega_m \beta(t) \boldsymbol{F_{msr}^r} - \boldsymbol{D_m} \boldsymbol{\dot{x}_m} - \gamma_m \boldsymbol{D_{m,h}} \boldsymbol{\dot{x}}_m \\ \boldsymbol{F_{ext}^r} = \omega_r \boldsymbol{K_c}(t) \boldsymbol{\tilde{x}_r} - \boldsymbol{D_c} \boldsymbol{\dot{x}_r} - \gamma_r \boldsymbol{D_{r,h}} \boldsymbol{\dot{x}_r} \end{cases} \tag{26}$$

It should be noted that the variable $\beta(t)(t_s < t < t_f)$, as defined in Eq.(9), serves as a smoothing factor for the force feedback during the initial activation of the pedal. During task execution, $\beta(t) = 1$. Subsequently, by integrating the time-varying energy stored in the tank from Eq. (20), the energy storage function of the system can be further expressed as:

$$V = T(s_t) + \frac{1}{2} \boldsymbol{\dot{x}_m^T} \boldsymbol{M_m} \boldsymbol{\dot{x}_m} + \frac{1}{2} \boldsymbol{\dot{x}_r^T} \boldsymbol{M_r} \boldsymbol{\dot{x}_r} \tag{27}$$

Deriving the energy storage function in Eq.(27), substituting Eq.(1) and Eq.(5) as well. Furthermore, leveraging the property that the Mass, Coriolis, and Centrifugal matrix $\left[\boldsymbol{\dot{M}}(\boldsymbol{x}) - 2\boldsymbol{C}(\boldsymbol{x}, \boldsymbol{\dot{x}})\right]$ is a skew-symmetric one [35], both the haptic device and the robotic manipulator, the following formulations can be obtained:

$$\begin{aligned} \dot{V} =& \dot{T}(s_t) + \frac{1}{2} \boldsymbol{\dot{x}_m^T} \boldsymbol{\dot{M}_m} \boldsymbol{\dot{x}_m} + \boldsymbol{\dot{x}_m^T} \boldsymbol{M_m} \boldsymbol{\ddot{x}_m} + \frac{1}{2} \boldsymbol{\dot{x}_r^T} \boldsymbol{\dot{M}_r} \boldsymbol{\dot{x}_r} + \boldsymbol{\dot{x}_r^T} \boldsymbol{M_r} \boldsymbol{\ddot{x}_r} \\ =& \dot{T}(s_t) + \frac{1}{2} \boldsymbol{\dot{x}_m^T} \boldsymbol{\dot{M}_m} \boldsymbol{\dot{x}_m} + \boldsymbol{\dot{x}_m^T} [\boldsymbol{F_{cmd}^m} + \boldsymbol{F_f^m} - \boldsymbol{C_m} \boldsymbol{\dot{x}_m}] \\ &+ \frac{1}{2} \boldsymbol{\dot{x}_r^T} \boldsymbol{\dot{M}_r} \boldsymbol{\dot{x}_r} + \boldsymbol{\dot{x}_r^T} [\boldsymbol{F_{cmd}^r} + \boldsymbol{F_{ext}^r} - \boldsymbol{C_r} \boldsymbol{\dot{x}_r}] \\ =& \dot{T}(s_t) + \frac{1}{2} \boldsymbol{\dot{x}_m^T} \cancel{[\boldsymbol{\dot{M}_m} - 2\boldsymbol{C_m}]} \boldsymbol{\dot{x}_m} + \boldsymbol{\dot{x}_m^T} [\boldsymbol{F_{cmd}^m} + \boldsymbol{F_f^m}] \\ &+ \frac{1}{2} \boldsymbol{\dot{x}_r^T} \cancel{[\boldsymbol{\dot{M}_r} - 2\boldsymbol{C_r}]} \boldsymbol{\dot{x}_r} + \boldsymbol{\dot{x}_r^T} [\boldsymbol{F_{cmd}^r} + \boldsymbol{F_{ext}^r}] \\ =& \dot{T}(s_t) + \boldsymbol{\dot{x}_m^T} \boldsymbol{F_{cmd}^m} + \boldsymbol{\dot{x}_m^T} \boldsymbol{F_f^m} + \boldsymbol{\dot{x}_r^T} \boldsymbol{F_{cmd}^r} + \boldsymbol{\dot{x}_r^T} \boldsymbol{F_{ext}^r} \end{aligned} \tag{28}$$

Afterwards, replacing the derivative of the energy $T(s_t)$ from Eq. (20) and Eq. (24). Moreover, considering the forces calculated using Eq.(26) and substituting the tank dynamics in Eq. (24), the following formulations can be obtained:

$$\begin{aligned} \dot{V} =& \dot{T}(s_t) + \boldsymbol{\dot{x}_m^T} \boldsymbol{F_{cmd}^m} + \boldsymbol{\dot{x}_m^T} [-\omega_m \boldsymbol{F_{msr}^r} - \boldsymbol{D_m} \boldsymbol{\dot{x}_m} - \gamma_m \boldsymbol{D_{m,h}} \boldsymbol{\dot{x}}_m] \\ &+ \boldsymbol{\dot{x}_r^T} \boldsymbol{F_{cmd}^r} + \boldsymbol{\dot{x}_r^T} [\omega_r \boldsymbol{K_c} \boldsymbol{\tilde{x}_r} - \boldsymbol{D_c} \boldsymbol{\dot{x}_r} - \gamma_r \boldsymbol{D_{r,h}} \boldsymbol{\dot{x}_r}] \\ =& \sigma_m \boldsymbol{\dot{x}_m^T} \boldsymbol{D_m} \boldsymbol{\dot{x}_m} + \sigma_r \boldsymbol{\dot{x}_r^T} \boldsymbol{D_c} \boldsymbol{\dot{x}_r} + \cancel{\omega_m \boldsymbol{\dot{x}_m^T} \boldsymbol{F_{msr}^r}} \\ &- \cancel{\omega_r \boldsymbol{\dot{x}_r^T} \boldsymbol{K_c} \boldsymbol{\tilde{x}_r}} + \cancel{\gamma_m \boldsymbol{\dot{x}_m^T} \boldsymbol{D_{m,h}} \boldsymbol{\dot{x}_m}} + \cancel{\gamma_r \boldsymbol{\dot{x}_r^T} \boldsymbol{D_{r,h}} \boldsymbol{\dot{x}_r}} \\ &+ \boldsymbol{\dot{x}_m^T} \boldsymbol{F_{cmd}^m} + \boldsymbol{\dot{x}_m^T} [\cancel{-\omega_m \boldsymbol{F_{msr}^r}} - \boldsymbol{D_m} \boldsymbol{\dot{x}_m} - \cancel{\gamma_m \boldsymbol{D_{m,h}} \boldsymbol{\dot{x}}_m}] \\ &+ \boldsymbol{\dot{x}_r^T} \boldsymbol{F_{cmd}^r} + \boldsymbol{\dot{x}_r^T} [\cancel{\omega_r \boldsymbol{K_c} \boldsymbol{\tilde{x}_r}} - \boldsymbol{D_c} \boldsymbol{\dot{x}_r} - \cancel{\gamma_r \boldsymbol{D_{r,h}} \boldsymbol{\dot{x}_r}}] \\ =& \sigma_m \boldsymbol{\dot{x}_m^T} \boldsymbol{D_m} \boldsymbol{\dot{x}_m} + \boldsymbol{\dot{x}_m^T} \boldsymbol{D_m} \boldsymbol{\dot{x}_m} + \sigma_r \boldsymbol{\dot{x}_r^T} \boldsymbol{D_c} \boldsymbol{\dot{x}_r} + \boldsymbol{\dot{x}_r^T} \boldsymbol{D_c} \boldsymbol{\dot{x}_r} \\ &+ \boldsymbol{\dot{x}_m^T} \boldsymbol{F_{cmd}^m} + \boldsymbol{\dot{x}_r^T} \boldsymbol{F_{cmd}^r} \\ =& \boldsymbol{\dot{x}_r} \boldsymbol{F_{cmd}^r} + \boldsymbol{\dot{x}_m} \boldsymbol{F_{cmd}^m} \\ &+ \underbrace{(\sigma_r - 1) \boldsymbol{\dot{x}_r}^T \boldsymbol{D_c} \boldsymbol{\dot{x}_r} + (\sigma_m - 1) \boldsymbol{\dot{x}_m^T} \boldsymbol{D_m} \boldsymbol{\dot{x}_m}}_{\leq 0} \end{aligned} \tag{29}$$

Considering $\sigma_m, \sigma_r \in \{0, 1\}$ by design (*Please refer to Eq. 22 for the details*) and $\boldsymbol{D_m}, \boldsymbol{D_c}$ as positive definite damping parameters, the last two terms are always negative. Consequently, the inequality in Eq. (29) holds, and the system's passivity condition presented in Eq. (10) can be guaranteed. It should be noted that the energy tank is implemented discretely in the physical robot system, which is expressed as below:

$$T(x_t) = T(x_{t-1}) + \dot{T}(x_t) \Delta t \tag{30}$$

where Δt is the sampling time step of the control loop.

2) Constraints to the controller: Subsequently, the energy constraint has been added to the QP-based optimization problem, which is expressed as:

- (iii) The energy, T, stored in the tank should always be regulated within the range of lower boundary, $\underline{E}$ and upper boundary, $\bar{E}$.

In this section, a global energy tank-based approach is introduced to address the stability challenges associated with teleoperated robot-assisted contact-rich tasks. This method ensures stability by imposing defined boundaries on the energy stored within the tank. Specifically, it modifies both the robot's active compliance and the bilateral teleoperation controller behavior, enhancing its capacity to maintain stability.

C. Passive Human-Robot Shared Control Strategy

As depicted in Fig.1, the robotic manipulator has been equipped with the tool for performing medical contact tasks. In surgical scenarios, the robot can be first teleoperated or programmed to approach the medical environment for task execution from the free space. Afterward, the robot is positioned close to the medical environment (e.g. on top of the phantom [1] or tissue), yet physical contact has not yet been established with the target anatomical structure. Afterwards, the initial pose of the robot $\boldsymbol{x_r}(t_0)$ is recorded, and the desired contact force, $\boldsymbol{F_{des}}$, is set based on the specific application scenario, ensuring an appropriate force level is set with the anatomical target.

Subsequently, the robot performs an (i) *"initialization"* step, aimed at achieving a static contact state with the medical environment, maintaining the desired force, $\boldsymbol{F_{des}}$, between the robot and the environment; (ii) Afterward, when the *"shared control loop"* is activated (the first time *"pedal on"*), the human operator controls the remote side robot position using the leader side haptic device as the input and incorporating the teleoperation control strategy delineated in Eq. (6) of Section III-C2. Meanwhile, the robot autonomously maintains the desired contact force $\boldsymbol{F_{des}}$ by actively shaping the robot stiffness $\boldsymbol{K_{opt}}(t)$, utilizing the QP-based optimization strategy (outlined later in Eq. (13) in Section IV-A). Specifically, the desired contact force aligns with the normal direction of the tissue or phantom model surface, which is required in various medical contact scenarios, e.g., ultrasound imaging, and palpation [55], [56]. In this way, the operator can effectively control the robot's position while enabling the robot to execute the contact-rich tasks simultaneously. Eventually, the details of the proposed active compliant and passive shared control strategy are summarized in Algorithm.2.

---

[1] In the medical context, the term *"phantom"* refers to a physical or virtual model that mimics the properties of human tissues, organs, or anatomical structures. It has been extensively utilized for various purposes, including medical testing, surgical training, simulation of physiological processes, etc.

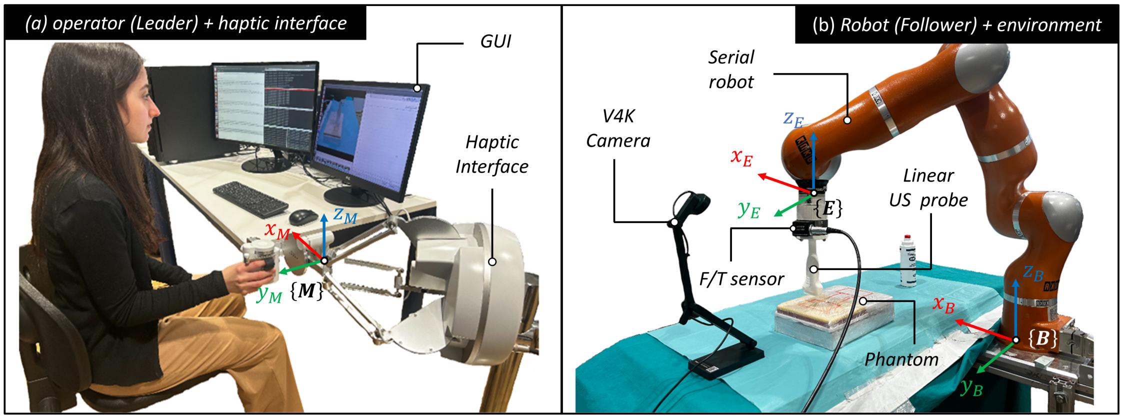

Fig. 3. System components of the proposed control framework. $\{\boldsymbol{M}\}$, $\{\boldsymbol{B}\}$, and $\{\boldsymbol{E}\}$ are the haptic interface (leader), robot base (follower), and the robot end effector coordinate systems, respectively. (a) The leader side, including a haptic interface, a desktop running the ROS package of the haptic interface and sending the command to the robot, and the GUI interface for visualization of the remote side environment; (b) The remote side, including a serial robot, a F/T sensor, a 3d printed linear probe, a web camera to capture the remote side information, and a phantom model.

Algorithm 2 Passive Human-Robot Shared Control Strategy

```
Input: Robot initial pose $x_r(t_0)$, desired force $F_{des}$, motion
       scaling parameter $\eta$, stiffness range $K_{min}$ and $K_{max}$.
Output: Desired position $x_r(t)$, optimal stiffness $K_{opt}$
Initialization: Static contact state with $F_{des}$ maintained
while shared-control loop is active do
    if pedal on then
        Update $x_r(t)$ using Eq.(6)
        Update $F^m_f(t)$ using Eq.(26)
    else
        $x_r(t) = x_r(0)$
        $F^m_f(t) = 0$
    end if
    if $\omega_r == 1$ then
        $K_c(t) = K_{opt}(t)$          ▷ Calculated by Eq. (13)
    else
        $K_c(t) = K_{min}$
    end if
    Update $\gamma_m, \gamma_r, \sigma_m, \sigma_r, \omega_m, \omega_r$ with Eq.(25), (22), (23)
end while
```

This section presents a human-robot shared control strategy designed to alleviate the physical and cognitive demands of the human operators during task execution. Specifically, the human operator provides high-level commands by manipulating a haptic device, while the proposed active compliant and passivity framework autonomously modulates the robot's behavior. This approach ensures effective task execution, maintaining system stability and safety.

V. EXPERIMENTAL SETUP

A. System Implementation

As shown in Fig.3, the developed system components primarily consist of the *"leader"* and *"follower"* sides.

1) Leader side: As illustrated in the left panel of Fig.3, the leader side comprises a haptic interface, a desktop computer running the ROS package associated with the haptic interface, which transmits commands to the robot, and a graphical user interface (GUI) for visualizing the environment on the remote robot side. The details of the components are listed below:

- A 7-DOFs haptic device Sigma.7 (Force Dimension, Switzerland), equipped with a switch pedal, is employed as the leader side haptic interface. Moreover, a custom-built ROS package[2] is adopted to acquire the position, velocity, and acceleration of the haptic interface and provide the human operator with haptic feedback with a control frequency at 1k Hz;
- Moreover, the QP-BLEIC (Boundary and Linear Equality Inequality Constrained) solver from the ALGLIB library[3] is adopted to solve the online QP optimization, using a desktop with Intel Core i9, 3.6 GHz, 16-core CPU, and 32 GB RAM;

2) Follower side: The right panel of Fig.3 gives the system components of the follower side, which include a serial robotic manipulator, a force/torque (F/T) sensor, a linear probe, an RGB webcam, and a phantom model.

- A 7-DOFs serial robotic manipulator, LWR IV+ (KUKA Roboter GmbH, Germany), incorporates the FastResearchInterface (FRI) Library and the ROS package[4], is employed to control the robot and perform the medical contact-rich tasks;
- A six-axis F/T sensor (M3815C-SN2537, SRI, China) is mounted to the robot end-effector to measure the contact force during task execution and has been calibrated;
- A 3D-printed linear ultrasound probe model (L12-5L40S-3, Telemed[5], Vilnius, Lithuania) is attached below the force sensor as the tool to mimic the contact scenario between the robot and medical environment;

B. Experimental Protocol

1) Material and Task description: ***Phantom materials***: As illustrated in Fig.4, considering the diverse anatomical target

---

[2] https://github.com/NEARLab-MedicalRobotics/Sigma-Interface
[3] https://www.alglib.net/quadratic-programming/
[4] https://github.com/CentroEPiaggio/kuka-lwr
[5] https://www.telemedultrasound.com/

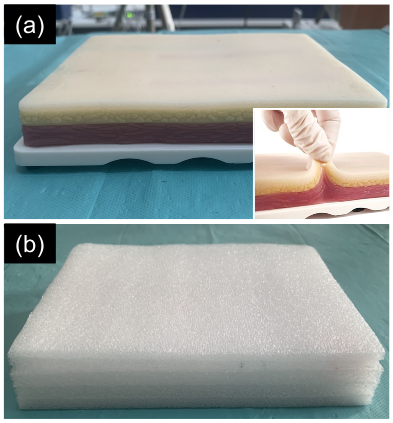

Fig. 4. Two phantoms adopted in the experiments [24], [57]. (a) soft silicone phantom to replicate the soft tissues, approximately [125, 500] N/m; (b) a polymeric foam to replicate harder anatomical structures, with stiffness approximately 4×10^3 N/m.

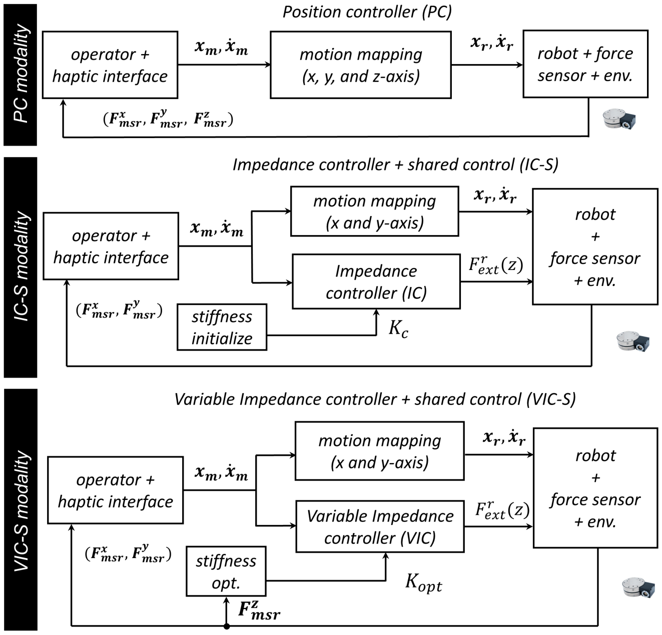
PC modality
Position controller (PC)
operator + haptic interface
$x_m, \dot{x}_m$
motion mapping (x, y, and z-axis)
$x_r, \dot{x}_r$
robot + force sensor + env.
$(F^x_{msr}, F^y_{msr}, F^z_{msr})$
IC-S modality
Impedance controller + shared control (IC-S)
operator + haptic interface
$x_m, \dot{x}_m$
motion mapping (x and y-axis)
$x_r, \dot{x}_r$
Impedance controller (IC)
$F^r_{ext}(z)$
robot + force sensor + env.
(F^x_{msr}, F^y_{msr})
stiffness initialize
K_c
VIC-S modality
Variable Impedance controller + shared control (VIC-S)
operator + haptic interface
$x_m, \dot{x}_m$
motion mapping (x and y-axis)
$x_r, \dot{x}_r$
Variable Impedance controller (VIC)
$F^r_{ext}(z)$
robot + force sensor + env.
(F^x_{msr}, F^y_{msr})
stiffness opt.
K_{opt}
F^z_{msr}

Fig. 5. Simplified schema of three control modalities in the experiment, namely *"PC"*, *"IC-S"*, and *"VIC-S"*, respectively.

characteristics inherent to the human body and spinal regions, two distinct phantom models, namely, the *Rigid* and *Soft* materials, are employed. ***Contact-rich tasks***: The tasks are designed to contact with a single *Rigid* and *Soft* material. Afterwards, the tasks are extended to sliding on the mimic anatomical structures that have distinct properties in real clinical scenarios, e.g., the intercostal Ultrasound imaging for biopsy or puncture where the rigid ribs and soft tissues are next to each other [58]. Specifically, tasks involving performing sliding from the Soft to Rigid (*Soft2Rigid*) materials and from the Rigid to Soft (*Rigid2Soft*) materials are implemented for the adaptability validation [59]. As depicted in Fig.3, the desired contact force, $\boldsymbol{F_{des}}$, is set normal to the tissue surface according to the real clinical protocol requirements [55], [56] (m=3 for the robot position control), which is along the z-axis w.r.t the robot end effector coordinate system $\{\boldsymbol{E}\}$.

TABLE I
CONTROLLER PARAMETERS IN THE EXPERIMENTS

Symbols	Values	Symbols	Values
Damping ratio ξ	0.71	F_{max}(N)	-20
Q	1×10^5	R	0.1
K_{min}(N/m)	100	K_{max}(N/m)	1×10^3
$\underline{E}$(J)	0.1	$\bar{E}$(J)	1.0
K_p	1.2	K_i	1.5
K_{con}(N/m)	500	Motion scaling η	0.15

2) Control Modalities: ***Position controller*** *(PC)*: As shown in Fig.5, a position-based teleoperation controller is employed by setting a high constant stiffness $diag\{3500, 3500, 3500\}$ N/m for the position and $diag\{250, 250, 250\}$ Nm/rad for the orientation of $\boldsymbol{K_{opt}}$. As depicted in Fig.3 (a), the operator performs all the defined tasks by manipulating the leader-side haptic device. Specifically, the desired contact force, $\boldsymbol{F_{des}}$ is adjusted by changing the robot's desired position $\boldsymbol{x_{rd}}$. In the meantime, the human operator can observe the measured force curve, $\boldsymbol{F_{msr}}$, by the F/T sensor displayed on the monitor.

Impedance controller with shared control strategy *(IC-S)*: The shared control framework presented in Section III-C2 is adopted and a constant robot stiffness value 500 N/m in Eq. (4) along the z-axis of $\boldsymbol{K_{opt}}$ is utilized. The robot stiffness along the x and y-axis and orientation stiffness of $\boldsymbol{K_{opt}}$ are the same as the values adopted in the *PC*-based modality. Notably, an offline *"one-step-perception"*[6] of the environment is implemented for setting a reasonable robot end effector displacement in Eq. (4) [24], [52], $\tilde{\boldsymbol{x}}$.

Variable impedance controller with shared control strategy *(VIC-S)*: In this modality, the proposed shared control framework in Section III-C2 incorporates the QP optimization and system passivity presented in Section IV-B is adopted. Similar to the other two modalities, the human operator controls the robot to contact the phantom while the robot stiffness along the z-axis of the optimal stiffness, $\boldsymbol{K_{opt}}$, is optimized by Eq.(13) to track the desired contact force. The detailed parameters of the proposed control framework are listed in Table.I.

3) Execution steps: To ensure fair comparisons, the robot is consistently programmed to initialize from the same starting position across all experimental setups. The steps of contact-rich task execution in the experiment are shown in Fig.6.

- ***Step 1-initialization***: The robot establishes contact with the environment from a pre-contact position and achieves the desired contact force, $\boldsymbol{F_{des}}$.
- ***Step 2-static contact***: The robot stays in a static position while keeping the contact, for several seconds.
- ***Step 3-sliding contact***: The operator is asked to perform the predefined tasks using the haptic interface and use the

---

[6] *one-step-perception:* This process involves using a Cartesian impedance controller with a constant stiffness, K_{con}, to contact the environment. Specifically, the robot is controlled to move along the tissue surface's normal direction, gradually changing the robot position to increase the force applied to the tissue until the predefined maximum contact force, $\boldsymbol{F_{max}}$, is reached. Subsequently, leveraging the data acquired during the *"one-step perception"* procedure, a reasonable displacement value in Eq.(4) can be set.

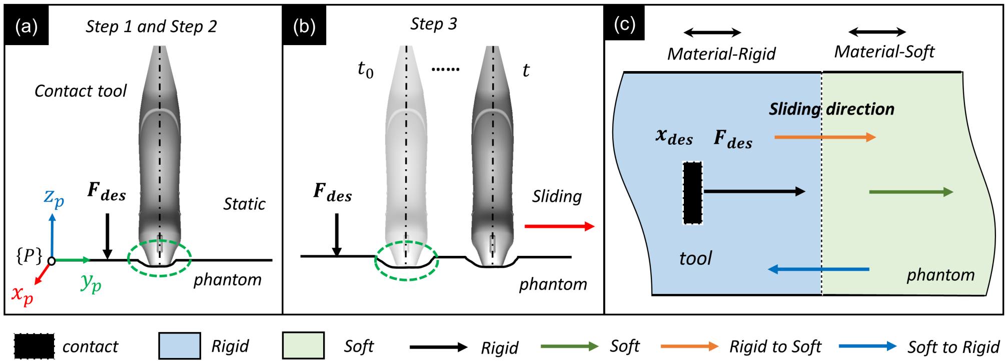

Fig. 6. Illustration of phases for desired force $\boldsymbol{F_{des}}$ tracking in medical contact task. (a) Contact phase-A: contact task along the normal direction and tracks desired contact force; (b) Contact Phase-B: contact task with both force tracking and sliding movement; (c) Illustration of contact and sliding on four different materials setups, sliding on (i) rigid material, (ii) soft material, (iii) from rigid to soft materials, (iv) from soft to rigid materials.

pedal to enable and disable the teleoperation control.

4) Experiments: ***Experiment 1 (E1):*** *System Assessment*. This experiment assesses the force-tracking capability of the proposed QP optimization-based controller outlined in Section IV-A. Specifically, both *constant* and *time-varying* desired contact force tracking tasks are implemented. Moreover, each setup is implemented with three repetitions. (i) In *constant force* setup, the robot is programmed to autonomously execute the medical contact-rich tasks with a constant desired contact force $\boldsymbol{F_{des}}$ and velocity of 10 mm/s, i.e., sliding on the surface of the phantom as shown in Fig.6. (ii) Furthermore, to investigate the force tracking performance utilizing the active compliant control strategy, two *time-varying* desired contact force tracking tasks are implemented, i.e., a *slope* reference force curve, $\boldsymbol{F_{slo}}$, and a *sinusoidal* reference force curve, $\boldsymbol{F_{sin}}$, which are formulated as below:

$$\boldsymbol{F_{slo}} = \begin{cases} -15 + 0.5t_1, & t_1 \in [10, 20] \\ 5 - 0.5t_2, & t_2 \in [20, 40] \\ -35 + 0.5t_3, & t_3 \in [40, 50] \end{cases} \tag{31}$$

$$\boldsymbol{F_{sin}} = -10 + 5\sin\left(\frac{2\pi}{40}(t-10)\right), t \in [10, 50] \tag{32}$$

Experiment 2 (E2): *Human-Robot Shared Control Framework Validation*. This experiment is designed to assess the performance of the proposed *VIC-S* framework and in contrast to the *PC* and *IC-S*-based modalities within the domain of teleoperated medical contact-rich tasks. To ensure a fair comparison, all the experiments are performed by the same human operator. Specifically, three different levels of desired contact forces, i.e., along the z-axis, are set in the experiment [24], $\boldsymbol{F_{des}} = -[5, 10, 15]$N. Moreover, each experiment setup is repeated seven times to facilitate statistical analysis.

Experiment 3 (E3): *Usability Evaluation*. $P = 12$ participants (8 males, 4 females, aged between 23-28 with avg = 25.4 and std = 1.5) were invited to perform the teleoperated medical contact-rich task with three control modalities, four materials, and three levels of desired contact forces. All participants were affiliated with the Politecnico di Milano, either as students or researchers specializing in biomedical engineering. Among them, six participants (two females and four males) reported prior experience with robotic systems. Additionally, three participants possessed experience with other teleoperation control systems. The ethics committee approved the experimental protocol from Politecnico di Milano, Italy (No.2023-5069). To avoid a learning curve and prevent unfair comparisons, participants are provided comprehensive instructions to familiarize themselves with the robotics system, the haptic interface, and the details of the experiment procedures before the experiments. Subsequently, each participant is allocated approximately 15 minutes to practice the contact tasks in all setups. In addition, each participant performs the predefined contact-rich tasks in a randomized sequence using the three control modalities. Then, the users were invited to fill out the NASA-TLX questionnaire [60] to evaluate their performance during the task execution.

C. Performance Metrics

(i) First, the Kolmogorov-Smirnov-Lilliefors test is exploited to check whether the data are normally distributed. The mean (MEA) and Standard Deviation (SD) values will be calculated for the normal distribution. Otherwise, the median (MED) and the interquartile range (IQR) values are calculated for the non-normal distribution of data [61].

(ii) To evaluate the force tracking performance, the MED and the IQR values of the desired force tracking error, F_{err} are reordered as E_{med} (N) and E_{iqr} (N), respectively. Moreover, the Root Mean Squared Error (RMSE) of the desired contact force, $\boldsymbol{F_{des}}$, during the task execution is recorded as F_{rmse} (N) and calculated as below:

$$F_{rmse} = \sqrt{\frac{1}{N}\sum_{i=0}^{N}(\boldsymbol{F^i_{msr}} - \boldsymbol{F_{des}})^2} \tag{33}$$

where $\boldsymbol{F^i_{msr}}$ represents the measured contact force by the force/torque sensor at the sampling time i.

(iii) During the tasks execution in ***E1*** and ***E2***, the optimal robot stiffness, $\boldsymbol{K_{opt}}$, and the energy, T, stored in the tank shouldn't violate the constraints and within the range of $[\boldsymbol{K_{min}}, \boldsymbol{K_{max}}]$ N/m and $[0.1, 1]$ J, respectively.

(iv) In addition, for the usability test in ***E3***, the users answered the NASA-TLX questionnaire after completing the

TABLE II
SUMMARY OF EXPERIMENT SETUPS, MATERIALS, PERFORMANCE METRICS, AND RESULTS

Experiments	Setups	Materials	Controller	Performance Metrics	Figures or Tables
E1	*Constant* desired force $(-[5, 10, 15])$ N	*Soft* *Rigid* *Soft2Rigid* *Rigid2Soft*	VIC	E_{med} [N] E_{iqr} [N] F_{rmse} [N]	Fig.7a and Fig.8
	Time-varying desired force $\boldsymbol{F_{slo}}$ (Eq.31), $\boldsymbol{F_{sin}}$ (Eq.32) [N]				Fig.7b and Fig.9
E2	*Constant* desired force $(-[5, 10, 15])$ N	*Soft* *Rigid* *Soft2Rigid* *Rigid2Soft*	PC IC-S VIC-S	Energy $\boldsymbol{T}$ [J] $\boldsymbol{K_{opt}}$ [N/m]	Fig.10
				E_{med} [N] E_{iqr} [N]	Fig.11
E3	*Constant* desired force $(-[5, 10, 15])$ N	*Soft* *Rigid* *Soft2Rigid* *Rigid2Soft*	PC IC-S VIC-S	E_{med} [N] E_{iqr} [N]	Fig.12
				NASA-TLX	Table.IV (Fig.13 and Fig.14)

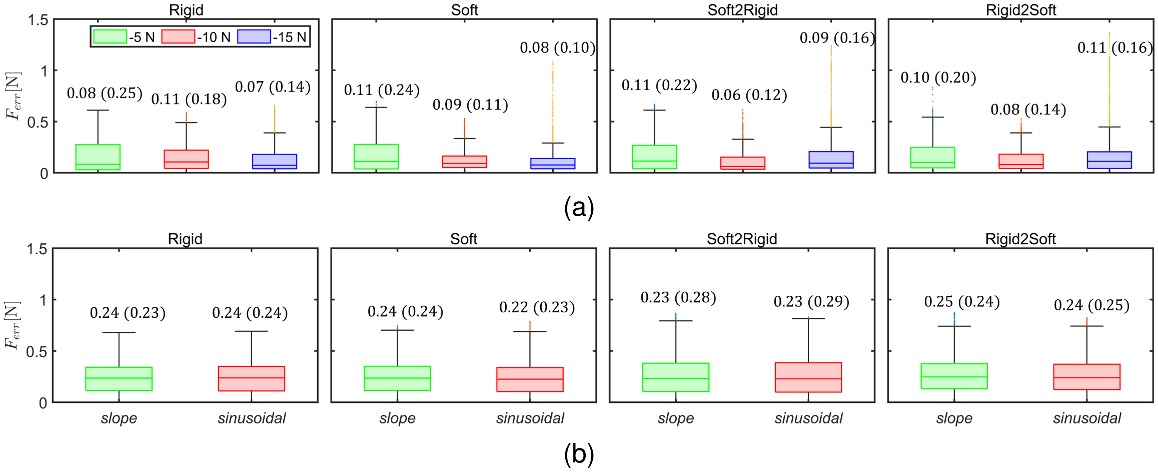

Fig. 7. E1 results with the boxplot of the desired force tracking errors. (a) Three constant reference forces, $\boldsymbol{F_{des}} = [-5, -10, -15]$N, on four different materials. 12 different setups are included, each with three repetitions. (b) E1 results with two time-varying reference forces, i.e., $\boldsymbol{F_{slo}}$ (Eq.31), $\boldsymbol{F_{sin}}$ (Eq.32).

task with each control modality, including the mental demand (MD), physical demand (PD), temporal demand (TD), performance (Pe), effort (Ef), and frustration (Fr) items. For each item, the score is in the range from 0 to 100 [60].

Moreover, the non-parametric statistical analysis is implemented to compare the results from different control modalities with the Wilcoxon Rank-Sum test exploited. Correspondingly, a significant difference is assessed with a $p - value < 0.05$, ($-$, $p \geq 0.05$ indicates that no significant difference exists. $*$, $p < 0.05$; $**$, $p < 0.01$; $***$, $p < 0.001$).

VI. EXPERIMENTAL RESULTS

The experiment setups, materials, control modalities, performance metrics, and figures are summarized in Table.II.

A. E1 Results: System Assessment Experiment

1) Constant force tracking results: As depicted in Fig.7a, the experiment results demonstrated the force tracking error boxplot when the robotic manipulator autonomously executes the predefined tasks. Specifically, the *Rigid* material contact task results are illustrated in panel 1 of Fig.7a and the statistical analysis reveals the E_{med} and E_{iqr} of the force tracking errors, $\boldsymbol{F_{err}}$, across the three levels of forces, i.e., -5N, -10N, and -15N, are calculated as 0.08(0.25) N, 0.11 (0.18) N, and 0.07 (0.14) N, respectively. Similarly, for the sliding contact tasks on *Soft* material shown in panel 2 of Fig.7a, the E_{med} and E_{iqr} values are calculated as 0.11 (0.24) N, 0.09 (0.11) N, and 0.08 (0.10) N, respectively. Furthermore, the E_{med} and E_{iqr} of force associated with contact tasks on the composite materials are reported as 0.11 (0.22) N, 0.06 (0.12) N, and 0.09 (0.16) N in the *Rigid2Soft* setup in panel 3 of Fig.7a and 0.10 (0.20) N, 0.08 (0.14) N, and 0.11 (0.16) N in the *Soft2Rigid* setup in panel 4 of Fig.7a, respectively.

Moreover, Fig.8 illustrated the details of the calculated optimal robot stiffness, $\boldsymbol{K_{opt}}$, under constant force conditions ranging from -5 to -15 N shown in Fig.7a. Specifically, as shown in the figures, spanning 0 to 10 seconds, the robot first implements the *"initialization"* phase to establish contact. During this phase, the robot stiffness is computed to be its maximum value of 1000 N/m, as the measured contact force, $\boldsymbol{F_{msr}}$, is at 0 N under the constraints of the optimization problem. Subsequently, the robot gradually decreased its stiffness as it interacted with the phantom, and the stiffness was not further updated when $\boldsymbol{F_{des}}$ was reached until the end of 10 seconds. Afterward, during the contact-rich tasks were

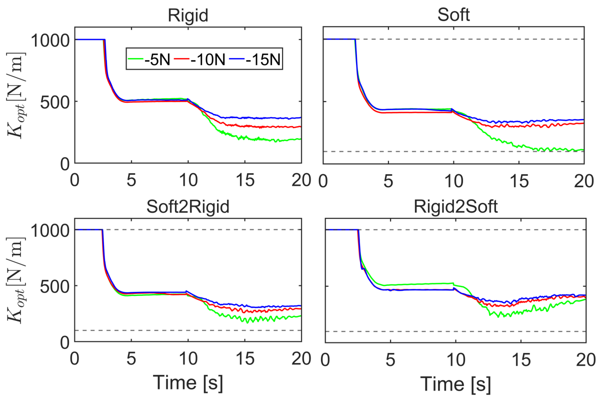

Fig. 8. E1 results of the optimal robot stiffness with constant reference forces contact task. (only one repetition is shown in the figure). From 0~10 seconds is the *"initialization"* phase. From 10~20 seconds is the *"sliding"* phase.

conducted until the end of 20 seconds, the robot stiffness was updated in real-time to track the desired contact forces.

2) Time-varying force tracking results: Fig.7b presents the results of the time-varying desired contact forces outlined in Eq.(31) and (32) in Section V-B. Firstly, the *initialization* is implemented to establish the contact. Afterward, during 0~40 seconds, by actively adjusting the stiffness value $\boldsymbol{K_{opt}}$, the robot is capable of tracking the desired force in both the *"slope"* and *"sinusoidal"* time-varying reference curves, as well as across single, i.e., *Rigid* and *Soft*, and composite phantom materials, i.e., *Soft2Rigid* and *Rigid2Soft*, setups. Table.III depicts the F_{rmse} during the *"slope"* and *"sinusoidal"* time-varying force tracking tasks.

Furthermore, in the context of time-varying contact force tracking, the sub-figures in Fig.9 depict the details of the optimal robot stiffness, $\boldsymbol{K_{opt}}$, and the measured contact force, $\boldsymbol{F_{msr}}$, in Fig.7b. Consistent with the findings presented in Fig.7a, the robot initially undergoes an *"initialization"* phase during the first 5 seconds, during which contact with the environment is established. Following this phase, the robot remains stationary for several seconds, during which the stiffness profile is held constant, ensuring the maintenance of the desired contact force. Subsequently, during the *"sliding"* phase across the phantom surface, the robot effectively tracks the desired contact forces, $\boldsymbol{F_{des}}$, in both the *"slope"* and *"sinusoidal"* cases. Additionally, it's important to highlight that in both constant force and time-varying desired contact force tracking scenarios, as depicted in Fig.8 and Fig.9, the robot stiffness stabilized at approximately 500 N/m following the completion of the *"initialization"* phase. This is primarily attributed to the implementation of the *"one-step perception"* strategy, which enabled the system to perceive the environmental characteristics without exceeding the stipulated stiffness constraints and, consequently, prevents the robot stiffness from approaching the boundaries of the predefined stiffness limits.

Consequently, the experiment results indicate the desired force-tracking capability using the proposed optimization-based variable impedance control method while maintaining stability during the contact-rich task execution, notwithstanding variations in environmental properties.

TABLE III
E1 RESULTS OF F_{rmse} [N] FOR DESIRED FORCE TRACKING

Materials	*Constant* $\boldsymbol{F_{des}}$			*Time-varying* $\boldsymbol{F_{des}}$	
	$-5N$	$-10N$	$-15N$	*slope*	*sinusoidal*
Rigid	0.22	0.19	0.21	0.27	0.24
Soft	0.24	0.17	0.24	0.28	0.27
Soft2Rigid	0.21	0.15	0.27	0.32	0.31
Rigid2Soft	0.20	0.17	0.29	0.33	0.31

B. E2 Results: Human-Robot Shared Control Validation

Fig.10 (a) to (d) illustrates the robot position displacement y_{msr}, the measured contact forces $\boldsymbol{F_{msr}}$, the optimal robot stiffness $\boldsymbol{K_{opt}}$ profiles, and the energy T stored in the tank, respectively, with the desired contact force $\boldsymbol{F_{des}} = -10N$ as an example [7] and exploiting *VIC-S* strategy. Specifically, the first phase T_1, $t \in [0, 5]$ seconds, constitutes the *"initialization"* period where the robot descends along the z-axis to achieve the desired contact force -10N. During this time, the human operator's teleoperation control is not activated. Moreover, the measured contact force (Fig.10 (b)) and the optimal robot stiffness (Fig.10 (c)) start with 0 N and the maximum value of 1000 N/m, respectively, since no contact occurred between the robot and the environment. Notably, Fig.10 (c) illustrates the real-time optimization of the robot stiffness profile $\boldsymbol{K_{opt}}$, facilitating a gradual convergence of the desired contact force around the 3 seconds. During $t \in [3, 5]$ seconds, the stiffness value of the robot in Fig.10 (c) does not change significantly anymore since the desired contact force is achieved. Furthermore, the energy stored in the tank depicted in Fig.10 (d) initializes at 0.1 J and stores the dissipated energy from the damping term, crucial for implementing the variable impedance control behaviors.

Afterward, during the phase T_2, $t \in [5, 10]$ seconds, the robot holds the current state for 5 seconds, and the force, stiffness, and energy stored in the task remain unchanged as shown in Fig.10. Subsequently, in phase T_3, from 10 seconds to the end, the teleoperation control is activated as shown in Fig.1 and Section III-C. During the *"sliding"* process using the proposed framework, as depicted in Fig.10 (a), the displacement command sent from the human operator on the leader side gradually increases to 10 cm, while the measured contact force, $\boldsymbol{F_{msr}}$, in Fig. 10 (b) exhibits minor fluctuations around the desired value, attributed to the dynamic sliding contact on the phantom model's surface and the online robot stiffness profile optimization for the contact task execution.

Moreover, Fig.11 presents the boxplot E_{med} and E_{iqr} of the force tracking errors, F_{err}, utilizing the *PC*, *IC-S*, and *VIC-S* control modalities across all experimental setups, with the constant desired contact force $\boldsymbol{F_{des}}$. Regarding the force tracking performance, the results depicted that the *VIC-S*-based control modality outperforms both the *PC* and *IC-*

---

[7] The results across all the desired contact forces are consistent. Considering the constraints on available space, only the results corresponding to -10N are presented in the manuscript. Detailed results for the other two force levels, -5N and -15N, are provided in the supplementary video.

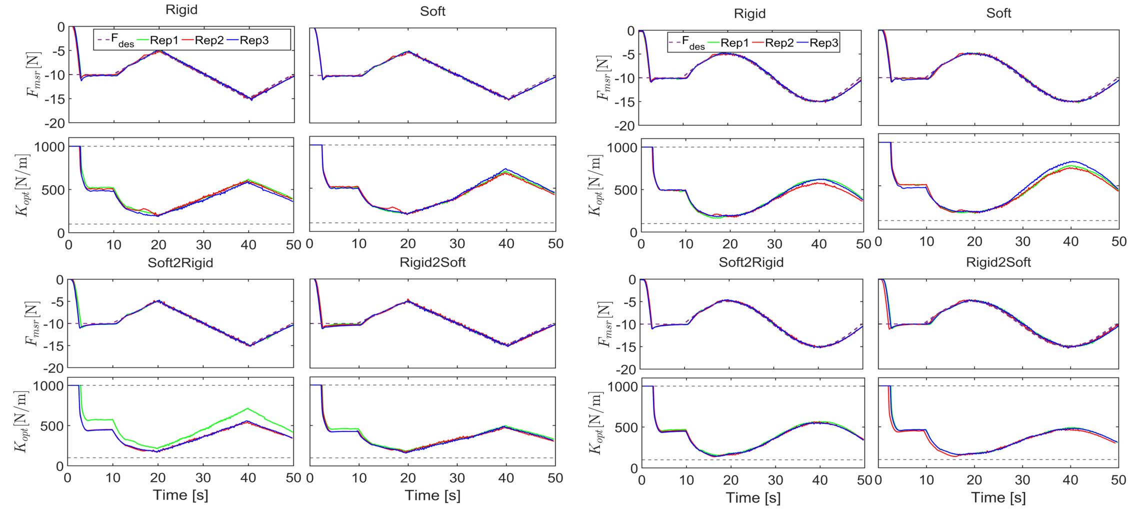

(a) (b)

Fig. 9. E1 results with time-varying reference forces in Fig.7b. (a) the *"slope"* time-varying reference force curve, and (b) the *"sinusoidal"* reference force curve. Specifically, from 0~10 seconds, the robot performs *"initialization"* and tracks the desired contact force, $\boldsymbol{F_{des}}$. Then, from 10~50 seconds, the robot performs the time-varying force-tacking task while sliding on the phantom along the y-axis.

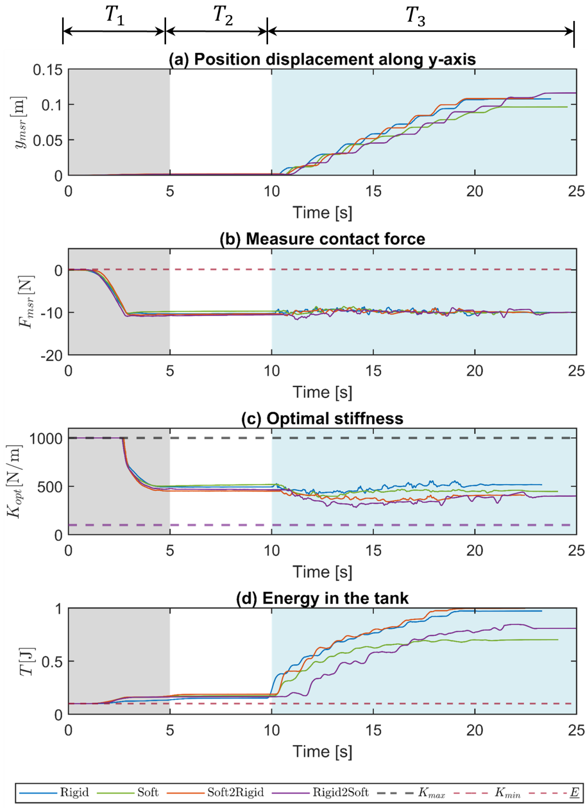

Fig. 10. E2 results with desired contact force $\boldsymbol{F_{des}} = -10N$ as an example. From top to bottom: the commanded robot displacement, y_{msr}, the measured contact force by the F/T sensor, F_{msr}, the optimal robot stiffness profile, $\boldsymbol{K_{opt}}$, and the energy in the tank, T, respectively. Specifically, 0~5 seconds is the *"initialization phase"* T_1, 5~10 seconds represents the *"static phase"* T_2, and 10 seconds to the end is the *"sliding phase"* T_3, respectively.

S-based control modalities. In Fig.11, the maximum E_{med} during the task execution across all the experiment setups are recorded as 0.91 N, 3.28 N, and 0.46 N for *IC*, *IC-S*, and *VIC-S*-based modalities, respectively. Furthermore, the maximum E_{iqr} values are reported as 1.82 N, 5.87 N, and 0.56 N, respectively. From the results, the significant E_{med} and E_{iqr} in *IC-S* control modality are observed, and this can be primarily attributed to the phantom not perfectly flat, and the simple *"one-step-perception"* of the phantom implemented solely at a specific point, where even minor positional deviations can lead to significant force errors. In contrast, as shown in Fig.10 and Fig.11, the proposed framework demonstrated robustness in addressing uneven conditions leveraging the QP-based variable impedance control strategy, thereby enhancing the adaptability of the execution of contacts-rich tasks. Furthermore, Fig.11 provides a comprehensive statistical analysis of the results and significant improvements in both E_{med} and E_{iqr} results can be found during the teleoperated contact-rich task execution in the comparison of *PC* vs *VIC-S* and *IC-S* vs *VIC-S* modalities.

The results of the human-robot shared control validation experiments demonstrated the effectiveness of the proposed control framework, particularly when compared to the *PC* and *IC-S* control modalities. Additionally, the energy stored in the system's energy tank consistently remains within the predefined lower and upper limits, thereby ensuring the passivity and stability of the overall system during the task execution.

C. E3 Results: Usability Evaluation

1) Quantitative evaluation results: Fig.12 depicts the results from 12 users during task execution, encompassing 36 distinct setups derived from combinations of four materials, three force levels, and three control modalities. Specifically, the results of E_{med} and E_{iqr} for the *PC*-based control modality revealed a notable standard deviation, highlighting the pronounced user-independent nature during the task execution. In addition, significant force tracking errors are observed due to the utilization of constant stiffness, $\boldsymbol{K_c}$, in the impedance controller Eq. (4). Hence, the proper and accurate

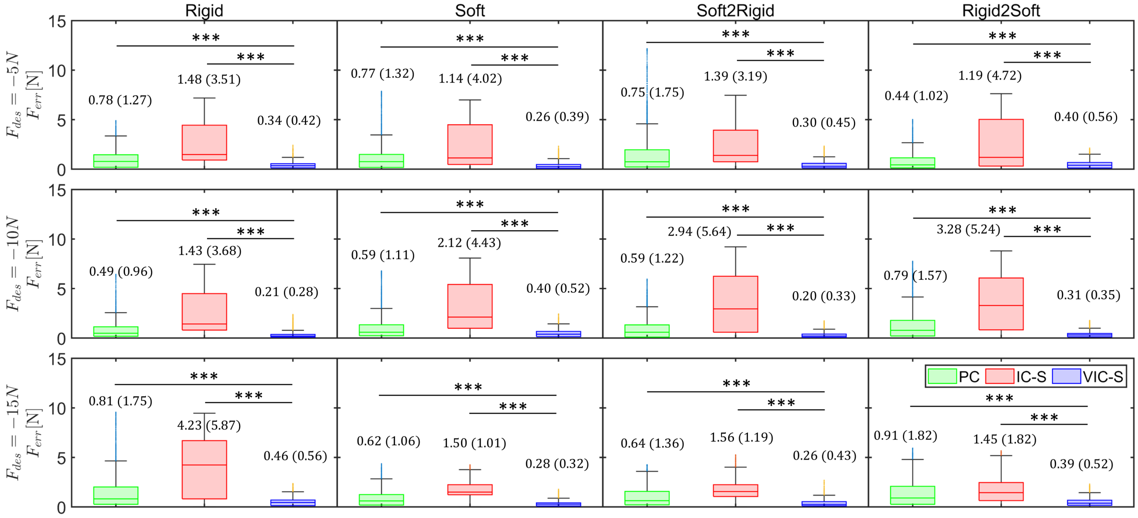

Fig. 11. E2 force tracking results. The green, red, and blue boxplots are the results for the control modalities *"PC"*, *"IC-S"*, and *"VIC-S"*, respectively.

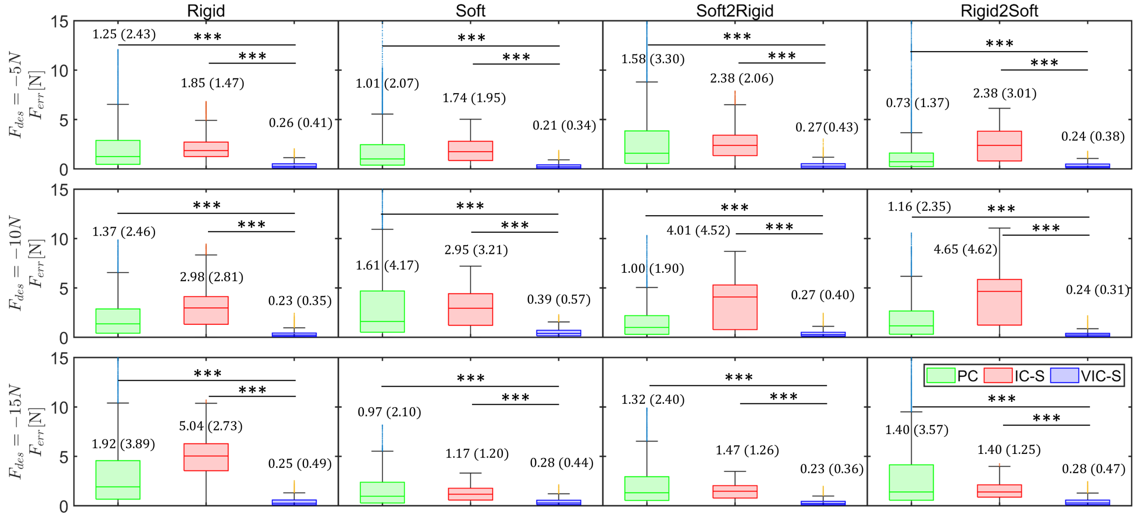

Fig. 12. E3 results with boxplots of force tracking error from 12 users. Specifically, the green, red, and blue boxplots represent the results for the control modalities *PC*, *IC-S* and *VIC-S*, respectively.

displacement, $\tilde{\boldsymbol{x}}_{\boldsymbol{r}}$, is typically needed for achieving considerable performance. On the other hand, substantial force errors are also attributed to the phantom not being perfectly flat. The *IC-S*-based approach cannot adapt to partially unknown environments during contact-rich task execution. Ultimately, as shown in Fig.12, the *VIC-S*-based control modality achieves the best performance in terms of desired contact force control and the variation of the results between the different users.

Furthermore, Fig.13 presents the measured contact force, $\boldsymbol{F_{msr}}$, during the task execution from 12 users with $\boldsymbol{F_{des}} = -10N$ as an example. Specifically, within the *PC*-based control modality, as shown in row 1, Fig.13, users engaged in manipulation of the haptic interface, adjusting contact force in real-time by observing the measured contact force, $\boldsymbol{F_{msr}}$, displayed on the GUI during the initialization phase T_1 from 0-5 seconds. Subsequently, the state is maintained for 5 seconds to sustain the desired contact force, as illustrated in phase T_2, revealing minimal force oscillations, which indicates that the users could handle the contact force in static contact tasks. However, significant oscillations of contact force occurred during the sliding process (10 seconds onwards, phase T_3), attributable to the concurrent execution of sliding and force control tasks, thereby imposing substantial demands on the operator. The experiment results also revealed that human operators performed better in maintaining the contact force in static contact tasks compared to sliding contact scenarios.

2) User evaluation results: The Kolmogorov-Smirnov-Lilliefors test reports that the user evaluation results are normal distribution. Furthermore, the user evaluation results and comparison results are depicted in Fig.14. Notably, significant differences between the *PC* vs *IC-S* and *PC* vs *VIC-S* comparison can be observed across all six NASA-TLX user evaluation items. Moreover, the user evaluation results and comparison results are depicted in Table IV. After rescaling the score within the range [0,100], the overall workload scores for *PC*, *IC-S*, and *VIC-S*-based modalities are reported as

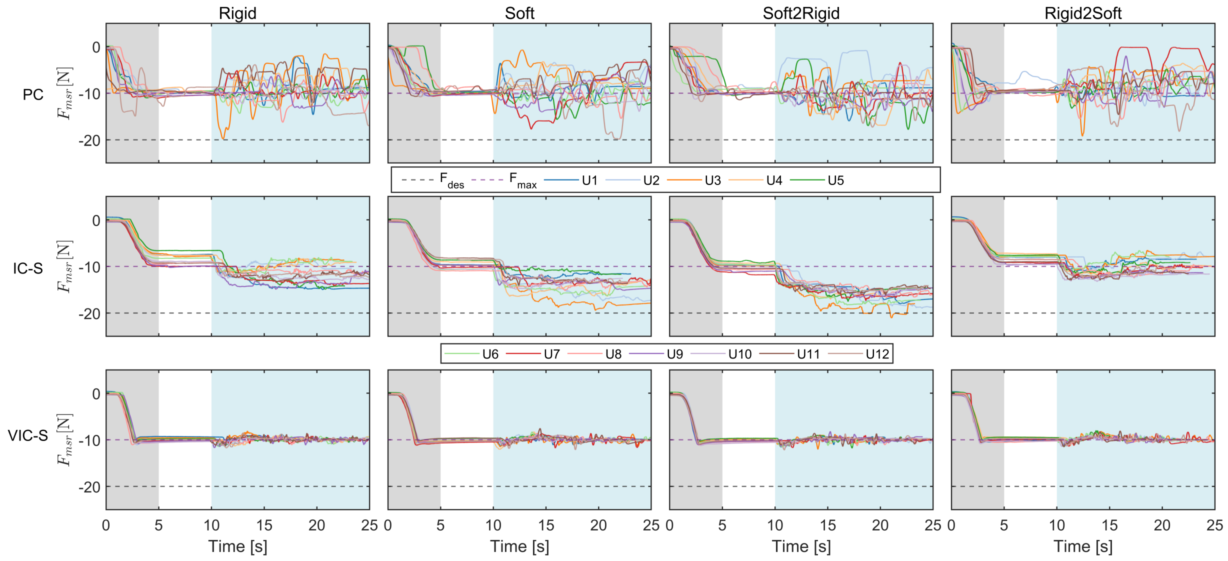

Fig. 13. E3 results of measured forces, $\boldsymbol{F_{msr}}$, during the task execution. U1 to U12 represent user 1 to user 12 in the experiment. 0~5 seconds, 5~10 seconds, and 10 seconds to the end are the *"initialization"* phase, *"static"* phase, and *"sliding contact"* phase, respectively.

83.33 ± 10.46, 40.00 ± 16.10, and 28.75 ± 15.50, respectively. Specifically, Table IV gives the detailed score of these items and reveals that the *VIC-S* control modality requires the lowest workload among the three modalities. The human subjective evaluation results demonstrated that the proposed shared control framework could significantly reduce the workload from the human operator during the teleoperated robot-assisted medical contact-rich task, both physically and mentally, compared to the conventional *PC*-based control modality.

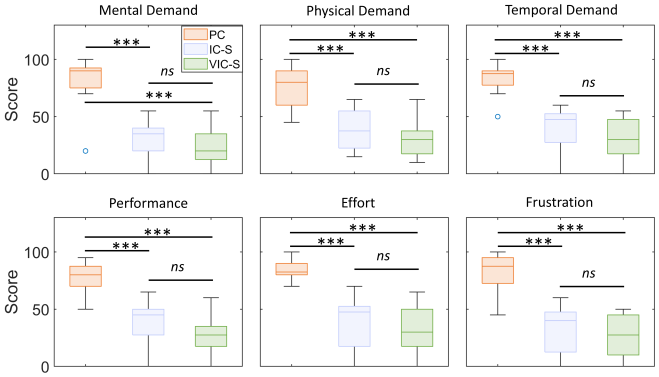

Fig. 14. User evaluation results with different modalities. *PC*, *IC-S*, and *VIC-S* are the *"position control"*, the *"impedance controller and shared control strategy"*, and *"variable impedance controller and shared control strategy"* modalities, respectively; ($*$, $p < 0.05$; $**$, $p < 0.01$; $***$, $p < 0.001$)

The user evaluation results demonstrate that the proposed framework significantly reduces the physical and cognitive workload experienced by human operators compared to the *PC*-based control paradigm. Furthermore, the *VIC-S*-based approach enhances task standardization in the execution of teleoperated robot-assisted contact-rich tasks, effectively minimizing operator-induced variability and ensuring more consistent task completion performance across different users.

TABLE IV
E3 NASA-TLX EVALUATION RESULTS (MEAN ± SD)

Items	Control Modalities		
	PC	*IC-S*	*VIC-S*
Mental	81.25 ± 20.53	31.67 ± 15.32	23.75 ± 14.31
Physical	75.42 ± 17.61	37.50 ± 17.14	30.83 ± 16.51
Temporal	82.92 ± 12.82	39.17 ± 17.66	30.42 ± 17.38
Performance	77.92 ± 13.30	39.16 ± 19.35	27.08 ± 16.51
Effort	84.58 ± 8.28	37.92 ± 22.12	32.08 ± 19.09
Frustration	80.83 ± 17.18	33.75 ± 19.05	26.67 ± 16.87
All	83.33 ± 10.46	40.00 ± 16.10	28.75 ± 15.50

VII. CONCLUSION

This work implemented an active compliant and passive human-robot shared control framework for teleoperated robot-assisted medical contact-rich tasks. The proposed framework aims to standardize task execution results, relieve the workload of medical staff, and enhance safety compared to conventional manual execution modality and constant stiffness impedance controller. Specifically, an online optimization approach, which incorporates the variable impedance control strategy using the QP optimization, was designed to facilitate force-tracking during contact-rich tasks. Moreover, a shared control schema that leverages the human operator input and the robot controller's autonomous force regulation capability was developed. Additionally, a global energy tank has been exploited to ensure the system's passivity. The experiment was conducted to verify the force-tracking performance, followed by the validation experiment and human subjective evaluation experiments. Experiment results demonstrated the superiority of the proposed framework when compared to the conventional manual position-based and constant stiffness-based force control modalities. Moreover, the human subjective evaluation results showcased that both the physical and mental workload imposed on human operators have been alleviated significantly.

Future works will focus on the test in more realistic environments considering human respiration and integrate medical images to monitor unexpected movements of phantom models and target anatomical structures. Furthermore, the redundancy of the robot can be exploited for multiple task execution, including hierarchical control, obstacle avoidance, manipulability optimization, and payload capabilities. Additionally, the quantitative evaluation of the human operator's workload during the experiment can be conducted by collecting and analyzing physiological measurements, including electroencephalography (EEG) [62], autonomic nervous system (ANS) responses, and surface electromyography (sEMG) [63], [64].

ACKNOWLEDGMENTS

The authors appreciate the contributions and constructive suggestions from the Editor-in-Chief, Associate Editor, and anonymous reviewers to help us significantly improve the manuscript. In addition, we would like to thank all the participants in the experiment.

APPENDIX

The details of the derivation of the equation, V, in Eq. (11) SectionIII-D to obtain Eq.(12) are given below:

$$
\begin{aligned}
\dot{V} =&\frac{1}{2}\dot{\boldsymbol{x}}_m^T \boldsymbol{M}_m \dot{\boldsymbol{x}}_m + \frac{1}{2}\dot{\boldsymbol{x}}_r^T \boldsymbol{M}_r \dot{\boldsymbol{x}}_r + \frac{1}{2}\tilde{\boldsymbol{x}}_r^T \boldsymbol{K}_c \tilde{\boldsymbol{x}}_r \\
=&\frac{1}{2}\dot{\boldsymbol{x}}_m^T \dot{\boldsymbol{M}}_m \dot{\boldsymbol{x}}_m + \dot{\boldsymbol{x}}_m^T \boldsymbol{M}_m \ddot{\boldsymbol{x}}_m + \frac{1}{2}\dot{\boldsymbol{x}}_r^T \dot{\boldsymbol{M}}_r \dot{\boldsymbol{x}}_r + \dot{\boldsymbol{x}}_r^T \boldsymbol{M}_r \ddot{\boldsymbol{x}}_r \\
&+ \frac{1}{2}\tilde{\boldsymbol{x}}_r^T \dot{\boldsymbol{K}}_c \tilde{\boldsymbol{x}}_r + \tilde{\boldsymbol{x}}_r^T \boldsymbol{K}_c \dot{\tilde{\boldsymbol{x}}}_r \\
=&\frac{1}{2}\dot{\boldsymbol{x}}_m^T \dot{\boldsymbol{M}}_m \dot{\boldsymbol{x}}_m + \dot{\boldsymbol{x}}_m^T [\boldsymbol{F}_{cmd}^m + \boldsymbol{F}_f^m - \boldsymbol{C}_m \dot{\boldsymbol{x}}_m] + \frac{1}{2}\dot{\boldsymbol{x}}_r^T \dot{\boldsymbol{M}}_r \dot{\boldsymbol{x}}_r \\
&+ \dot{\boldsymbol{x}}_r^T [\boldsymbol{F}_{cmd}^r + \boldsymbol{F}_{ext}^r - \boldsymbol{C}_r \dot{\boldsymbol{x}}_r] + \frac{1}{2}\tilde{\boldsymbol{x}}_r^T \dot{\boldsymbol{K}}_c \tilde{\boldsymbol{x}}_r + \tilde{\boldsymbol{x}}_r^T \boldsymbol{K}_c \dot{\tilde{\boldsymbol{x}}}_r \\
=&\frac{1}{2}\dot{\boldsymbol{x}}_m^T \cancel{[\dot{\boldsymbol{M}}_m - 2\boldsymbol{C}_m]} \dot{\boldsymbol{x}}_m + \dot{\boldsymbol{x}}_m^T [\boldsymbol{F}_{cmd}^m - \boldsymbol{F}_{msr}^r - \boldsymbol{D}_m \dot{\boldsymbol{x}}_m] \\
&+ \frac{1}{2}\dot{\boldsymbol{x}}_r^T \cancel{[\dot{\boldsymbol{M}}_r - 2\boldsymbol{C}_r]} \dot{\boldsymbol{x}}_r + \dot{\boldsymbol{x}}_r^T [\boldsymbol{F}_{cmd}^r + \cancel{\boldsymbol{K}_c \tilde{\boldsymbol{x}}_r} - \boldsymbol{D}_c \dot{\boldsymbol{x}}_r] \\
&+ \frac{1}{2}\tilde{\boldsymbol{x}}_r^T \dot{\boldsymbol{K}}_c \tilde{\boldsymbol{x}}_r + \tilde{\boldsymbol{x}}_r^T \boldsymbol{K}_c [\dot{\boldsymbol{x}}_{rd} - \cancel{\dot{\boldsymbol{x}}_r}] \\
=&\dot{\boldsymbol{x}}_r^T \boldsymbol{F}_{cmd}^r - \dot{\boldsymbol{x}}_r^T \boldsymbol{D}_c \dot{\boldsymbol{x}}_r + \dot{\boldsymbol{x}}_m^T \boldsymbol{F}_{cmd}^m - \dot{\boldsymbol{x}}_m^T \boldsymbol{D}_m \dot{\boldsymbol{x}}_m \\
&+ \frac{1}{2}\tilde{\boldsymbol{x}}_r^T \dot{\boldsymbol{K}}_c \tilde{\boldsymbol{x}}_r + \dot{\boldsymbol{x}}_{rd}^T \boldsymbol{K}_c \tilde{\boldsymbol{x}}_r - \dot{\boldsymbol{x}}_m^T \boldsymbol{F}_{msr}^r
\end{aligned}
\tag{34}
$$

REFERENCES

[1] E. De Momi and A. Segato, "Autonomous robotic surgery makes light work of anastomosis," *Science robotics*, vol. 7, no. 62, p. eabn6522, 2022.

[2] P. E. Dupont, B. J. Nelson, M. Goldfarb, B. Hannaford, A. Menciassi, M. K. O'Malley, N. Simaan, P. Valdastri, and G.-Z. Yang, "A decade retrospective of medical robotics research from 2010 to 2020," *Science robotics*, vol. 6, no. 60, p. eabi8017, 2021.

[3] C. C. Nguyen, S. Wong, M. T. Thai, T. T. Hoang, P. T. Phan, J. Davies, L. Wu, D. Tsai, H.-P. Phan, N. H. Lovell *et al.*, "Advanced user interfaces for teleoperated surgical robotic systems," *Advanced Sensor Research*, vol. 2, no. 4, p. 2200036, 2023.

[4] A. Attanasio, B. Scaglioni, E. De Momi, P. Fiorini, and P. Valdastri, "Autonomy in surgical robotics," *Annual Review of Control, Robotics, and Autonomous Systems*, vol. 4, pp. 651–679, 2021.

[5] P. Fiorini, K. Y. Goldberg, Y. Liu, and R. H. Taylor, "Concepts and trends in autonomy for robot-assisted surgery," *Proc. IEEE*, vol. 110, no. 7, pp. 993–1011, 2022.

[6] M. Selvaggio, R. Moccia, F. Ficuciello, B. Siciliano *et al.*, "Haptic-guided shared control for needle grasping optimization in minimally invasive robotic surgery," in *2019 IEEE/RSJ International Conference on Intelligent Robots and Systems (IROS)*, pp. 3617–3623. IEEE, 2019.

[7] I. Tamadon, S. H. Sadati, V. Mamone, V. Ferrari, C. Bergeles, and A. Menciassi, "Semiautonomous robotic manipulator for minimally invasive aortic valve replacement," *IEEE Transactions on Robotics*, 2023.

[8] Y. Yan and J. Pan, "Fast localization and segmentation of tissue abnormalities by autonomous robotic palpation," *IEEE Robotics and Automation Letters*, vol. 6, no. 2, pp. 1707–1714, 2021.

[9] Z. Jiang, S. E. Salcudean, and N. Navab, "Robotic ultrasound imaging: State-of-the-art and future perspectives," *Medical image analysis*, p. 102878, 2023.

[10] L. He, N. Herzig, S. de Lusignan, L. Scimeca, P. Maiolino, F. Iida, and T. Nanayakkara, "An abdominal phantom with tunable stiffness nodules and force sensing capability for palpation training," *IEEE Transactions on Robotics*, vol. 37, no. 4, pp. 1051–1064, 2020.

[11] A. Pappalardo, A. Albakri, C. Liu, L. Bascetta, E. De Momi, and P. Poignet, "Hunt–crossley model based force control for minimally invasive robotic surgery," *Biomedical Signal Processing and Control*, vol. 29, pp. 31–43, 2016.

[12] D. Huang, C. Yang, M. Zhou, A. Karlas, N. Navab, and Z. Jiang, "Robot-assisted deep venous thrombosis ultrasound examination using virtual fixture," *IEEE Transactions on Automation Science and Engineering*, 2024.

[13] M. Breunig, A. Hanson, and M. Huckabee, "Learning curves for point-of-care ultrasound image acquisition for novice learners in a longitudinal curriculum," *The Ultrasound Journal*, vol. 15, no. 1, p. 31, 2023.

[14] G. Harrison and A. Harris, "Work-related musculoskeletal disorders in ultrasound: Can you reduce risk?" *Ultrasound*, vol. 23, no. 4, pp. 224–230, 2015.

[15] J. Zhu, A. Cherubini, C. Dune, D. Navarro-Alarcon, F. Alambeigi, D. Berenson, F. Ficuciello, K. Harada, J. Kober, X. Li *et al.*, "Challenges and outlook in robotic manipulation of deformable objects," *IEEE Robotics & Automation Magazine*, vol. 29, no. 3, pp. 67–77, 2022.

[16] F. Liu, Z. Li, Y. Han, J. Lu, F. Richter, and M. C. Yip, "Real-to-sim registration of deformable soft tissue with position-based dynamics for surgical robot autonomy," in *2021 IEEE International Conference on Robotics and Automation (ICRA)*, pp. 12 328–12 334. IEEE, 2021.

[17] A. E. Abdelaal, P. Mathur, and S. E. Salcudean, "Robotics in vivo: A perspective on human–robot interaction in surgical robotics," *Annual Review of Control, Robotics, and Autonomous Systems*, vol. 3, pp. 221–242, 2020.

[18] G. Averta and N. Hogan, "Enhancing robot-environment physical interaction via optimal impedance profiles," in *2020 8th IEEE RAS/EMBS International Conference for Biomedical Robotics and Biomechatronics (BioRob)*, pp. 973–980. IEEE, 2020.

[19] M. W. Gilbertson and B. W. Anthony, "Force and position control system for freehand ultrasound," *IEEE Transactions on Robotics*, vol. 31, no. 4, pp. 835–849, 2015.

[20] Y. Sun and T. C. Lueth, "Safe manipulation in robotic surgery using compliant constant-force mechanism," *IEEE Transactions on Medical Robotics and Bionics*, 2023.

[21] T. Li, H. Xing, H. D. Taghirad, and M. Tavakoli, "Emg-based hybrid impedance-force control for human-robot collaboration on ultrasound imaging," in *2022 IEEE/RSJ International Conference on Intelligent Robots and Systems (IROS)*, pp. 670–675. IEEE, 2022.

[22] N. Hogan, "Impedance control: An approach to manipulation," in *1984 American control conference*, pp. 304–313. IEEE, 1984.

[23] F. Ficuciello, L. Villani, and B. Siciliano, "Variable impedance control of redundant manipulators for intuitive human–robot physical interaction," *IEEE Transactions on Robotics*, vol. 31, no. 4, pp. 850–863, 2015.

[24] Z. Jiang, Y. Zhou, Y. Bi, M. Zhou, T. Wendler, and N. Navab, "Deformation-aware robotic 3d ultrasound," *IEEE Robotics and Automation Letters*, vol. 6, no. 4, pp. 7675–7682, 2021.

[25] L. Wijayarathne, Z. Zhou, Y. Zhao, and F. L. Hammond, "Real-time deformable-contact-aware model predictive control for force-modulated manipulation," *IEEE Transactions on Robotics*, 2023.

[26] L. Roveda, N. Iannacci, F. Vicentini, N. Pedrocchi, F. Braghin, and L. M. Tosatti, "Optimal impedance force-tracking control design with

impact formulation for interaction tasks," *IEEE Robotics and Automation Letters*, vol. 1, no. 1, pp. 130–136, 2015.

[27] A. Duan, M. Victorova, J. Zhao, Y. Sun, Y. Zheng, and D. Navarro-Alarcon, "Ultrasound-guided assistive robots for scoliosis assessment with optimization-based control and variable impedance," *IEEE Robotics and Automation Letters*, vol. 7, no. 3, pp. 8106–8113, 2022.

[28] G. Ning, H. Liang, X. Zhang, and H. Liao, "Inverse-reinforcement-learning-based robotic ultrasound active compliance control in uncertain environments," *IEEE Transactions on Industrial Electronics*, 2023.

[29] D. Wu, X. T. Ha, Y. Zhang, M. Ourak, G. Borghesan, K. Niu, F. Trauzettel, J. Dankelman, A. Menciassi, and E. Vander Poorten, "Deep-learning-based compliant motion control of a pneumatically-driven robotic catheter," *IEEE Robotics and Automation Letters*, vol. 7, no. 4, pp. 8853–8860, 2022.

[30] J. Lachner, F. Allmendinger, E. Hobert, N. Hogan, and S. Stramigioli, "Energy budgets for coordinate invariant robot control in physical human–robot interaction," *The International Journal of Robotics Research*, vol. 40, no. 8-9, pp. 968–985, 2021.

[31] S. Stramigioli, "Energy-aware robotics," in *Mathematical control theory I: Nonlinear and hybrid control systems*, pp. 37–50. Springer, 2015.

[32] P. Paik, S. Thudi, and S. F. Atashzar, "Power-based velocity-domain variable structure passivity signature control for physical human-(tele) robot interaction," *IEEE Transactions on Robotics*, vol. 39, no. 1, pp. 386–398, 2022.

[33] T. Kastritsi and Z. Doulgeri, "A passive control framework for a bilateral leader-follower robotic surgical setup imposing rcm and active constraints," in *2022 IEEE/RSJ International Conference on Intelligent Robots and Systems (IROS)*, pp. 1175–1181. IEEE, 2022.

[34] F. Califano, R. Rashad, C. Secchi, and S. Stramigioli, "On the use of energy tanks for robotic systems," in *International Workshop on Human-Friendly Robotics*, pp. 174–188. Springer, 2022.

[35] F. Ferraguti, C. Secchi, and C. Fantuzzi, "A tank-based approach to impedance control with variable stiffness," in *2013 IEEE international conference on robotics and automation*, pp. 4948–4953. IEEE, 2013.

[36] X. Bao, S. Wang, R. Housden, J. Hajnal, and K. Rhode, "A constant-force end-effector with online force adjustment for robotic ultrasonography," *IEEE robotics and automation letters*, vol. 6, no. 2, pp. 2547–2554, 2021.

[37] F. Benzi, F. Ferraguti, G. Riggio, and C. Secchi, "An energy-based control architecture for shared autonomy," *IEEE Transactions on Robotics*, vol. 38, no. 6, pp. 3917–3935, 2022.

[38] Y. Michel, C. Ott, and D. Lee, "Safety-aware hierarchical passivity-based variable compliance control for redundant manipulators," *IEEE Transactions on Robotics*, vol. 38, no. 6, pp. 3899–3916, 2022.

[39] M. Franken, S. Stramigioli, S. Misra, C. Secchi, and A. Macchelli, "Bilateral telemanipulation with time delays: A two-layer approach combining passivity and transparency," *IEEE transactions on robotics*, vol. 27, no. 4, pp. 741–756, 2011.

[40] M. Minelli, F. Ferraguti, N. Piccinelli, R. Muradore, and C. Secchi, "An energy-shared two-layer approach for multi-master-multi-slave bilateral teleoperation systems," in *2019 International Conference on Robotics and Automation (ICRA)*, pp. 423–429. IEEE, 2019.

[41] F. Ferraguti, N. Preda, A. Manurung, M. Bonfe, O. Lambercy, R. Gassert, R. Muradore, P. Fiorini, and C. Secchi, "An energy tank-based interactive control architecture for autonomous and teleoperated robotic surgery," *IEEE Transactions on Robotics*, vol. 31, no. 5, pp. 1073–1088, 2015.

[42] Y. Michel, R. Rahal, C. Pacchierotti, P. R. Giordano, and D. Lee, "Bilateral teleoperation with adaptive impedance control for contact tasks," *IEEE Robotics and Automation Letters*, vol. 6, no. 3, pp. 5429–5436, 2021.

[43] A. Dietrich, X. Wu, K. Bussmann, C. Ott, A. Albu-Schäffer, and S. Stramigioli, "Passive hierarchical impedance control via energy tanks," *IEEE Robotics and Automation Letters*, vol. 2, no. 2, pp. 522–529, 2016.

[44] V. R. Garate, S. Gholami, and A. Ajoudani, "A scalable framework for multi-robot tele-impedance control," *IEEE Transactions on Robotics*, vol. 37, no. 6, pp. 2052–2066, 2021.

[45] M. Takeuchi, Y. Hironaka, T. Aoyama, and Y. Hasegawa, "Intuitive remote robotic nasal sampling by orientation control with variable rcm in limited space," *IEEE Transactions on Medical Robotics and Bionics*, vol. 4, no. 3, pp. 646–655, 2022.

[46] M. Selvaggio, J. Cacace, C. Pacchierotti, F. Ruggiero, and P. R. Giordano, "A shared-control teleoperation architecture for nonprehensile object transportation," *IEEE Transactions on Robotics*, vol. 38, no. 1, pp. 569–583, 2021.

[47] G. Li, Q. Li, C. Yang, Y. Su, Z. Yuan, and X. Wu, "The classification and new trends of shared control strategies in telerobotic systems: A survey," *IEEE Transactions on Haptics*, 2023.

[48] R. Rahal, G. Matarese, M. Gabiccini, A. Artoni, D. Prattichizzo, P. R. Giordano, and C. Pacchierotti, "Caring about the human operator: haptic shared control for enhanced user comfort in robotic telemanipulation," *IEEE transactions on haptics*, vol. 13, no. 1, pp. 197–203, 2020.

[49] M. Jorda, M. Vulliez, and O. Khatib, "Local autonomy-based haptic-robot interaction with dual-proxy model," *IEEE Transactions on Robotics*, vol. 38, no. 5, pp. 2943–2961, 2022.

[50] B. Siciliano, L. Sciavicco, L. Villani, and G. Oriolo, *Robotics: Modelling, Planning and Control*. Springer, 2008.

[51] C. Ott, *Cartesian impedance control of redundant and flexible-joint robots*. Springer, 2008.

[52] J. Tan, Y. Li, B. Li, Y. Leng, J. Peng, J. Wu, B. Luo, X. Chen, Y. Rong, and C. Fu, "Automatic generation of autonomous ultrasound scanning trajectory based on 3-d point cloud," *IEEE Transactions on Medical Robotics and Bionics*, vol. 4, no. 4, pp. 976–990, 2022.

[53] T. Hatanaka, N. Chopra, M. Fujita, and M. W. Spong, *Passivity-based control and estimation in networked robotics*. Springer, 2015.

[54] S. Fahmi, M. Focchi, A. Radulescu, G. Fink, V. Barasuol, and C. Semini, "Stance: Locomotion adaptation over soft terrain," *IEEE Transactions on Robotics*, vol. 36, no. 2, pp. 443–457, 2020.

[55] R. Goel, F. Abhimanyu, K. Patel, J. Galeotti, and H. Choset, "Autonomous ultrasound scanning using bayesian optimization and hybrid force control," in *2022 International Conference on Robotics and Automation (ICRA)*, pp. 8396–8402. IEEE, 2022.

[56] K. Su, J. Liu, X. Ren, Y. Huo, G. Du, W. Zhao, X. Wang, B. Liang, D. Li, and P. X. Liu, "A fully autonomous robotic ultrasound system for thyroid scanning," *Nature Communications*, vol. 15, no. 1, p. 4004, 2024.

[57] C. Hennersperger, B. Fuerst, S. Virga, O. Zettinig, B. Frisch, T. Neff, and N. Navab, "Towards mri-based autonomous robotic us acquisitions: a first feasibility study," *IEEE transactions on medical imaging*, vol. 36, no. 2, pp. 538–548, 2016.

[58] R. Göbl, S. Virga, J. Rackerseder, B. Frisch, N. Navab, and C. Hennersperger, "Acoustic window planning for ultrasound acquisition," *International journal of computer assisted radiology and surgery*, vol. 12, pp. 993–1001, 2017.

[59] D. G. Raitt, M. Huseynov, S. Homer-Vanniasinkam, H. A. Wurdemann, and S.-A. Abad, "Soft-tipped sensor with compliance control for elasticity sensing and palpation," *IEEE Transactions on Robotics*, 2024.

[60] S. G. Hart, "Nasa-task load index (nasa-tlx); 20 years later," in *Proceedings of the human factors and ergonomics society annual meeting*, vol. 50, no. 9, pp. 904–908. Sage publications Sage CA: Los Angeles, CA, 2006.

[61] X. Zhang, A. Sridhar, X. T. Ha, S. Z. Mehdi, A. Fortuna, M. Magro, A. Peloso, A. Bicchi, M. Ourak, A. Aliverti *et al.*, "Path tracking control of a steerable catheter in transcatheter cardiology interventions," *International Journal of Computer Assisted Radiology and Surgery*, pp. 1–10, 2024.

[62] D. Novak, B. Beyeler, X. Omlin, and R. Riener, "Workload estimation in physical human–robot interaction using physiological measurements," *Interacting with computers*, vol. 27, no. 6, pp. 616–629, 2015.

[63] M. Lorenzini, W. Kim, E. De Momi, and A. Ajoudani, "A new overloading fatigue model for ergonomic risk assessment with application to human-robot collaboration," in *2019 International Conference on Robotics and Automation (ICRA)*, pp. 1962–1968. IEEE, 2019.

[64] S. K. Hopko, R. Khurana, R. K. Mehta, and P. R. Pagilla, "Effect of cognitive fatigue, operator sex, and robot assistance on task performance metrics, workload, and situation awareness in human-robot collaboration," *IEEE Robotics and Automation Letters*, vol. 6, no. 2, pp. 3049–3056, 2021.

Junling Fu (Graduate Student Member, IEEE) received his B.E. degree in Mechanical Engineering from Guangzhou University, China, in 2017, and his M.E. degree in Mechanical Engineering from South China University of Technology, China, in 2020. In 2024, he completed his PhD in the Department of Electronics, Information, and Bioengineering (DEIB) at Politecnico di Milano, Italy, where he works as a postdoctoral researcher. During his PhD studies, he was a visiting PhD student at the Chair for Computer Aided Medical Procedures & Augmented Reality (CAMP) at the Technical University of Munich, Germany.

His research interests include medical robotics, human-robot interaction and collaboration, virtual/augmented/mixed reality, haptic-based teleoperation control, shared control, and robot learning.

Giorgia Maimone received her B.S. and M.S. degrees in Biomedical Engineering from Politecnico di Milano, Milan, Italy, in 2021 and 2024 respectively.

Her research interests include medical robotics, human-robot shared control frameworks, variable impedance control, and bilateral teleoperation.

Elisa Iovene (Graduate Student Member, IEEE) received her M.E. degree in Biomedical Engineering from Politecnico di Milano, Milan, Italy, in 2021. In 2024, she completed her PhD in the Department of Electronics, Information, and Bioengineering (DEIB) at Politecnico di Milano, Italy. Currently, she is a Postdoctoral Researcher at the Neuroengineering and Medical Robotics Laboratory, Medical Robotics Section (NEARLab, MRS).

Her research focuses on medical robotics, human-robot interaction and collaboration, autonomous navigation, and shared control, with a particular emphasis on the neurosurgical domain.

Jianzhuang Zhao (Graduate Student Member, IEEE) received his PhD from the Italian Institute of Technology and Politecnico di Milano, Italy, in 2024. Previously, he earned his B.Eng degree in mechanical engineering from Zhengzhou University, Zhengzhou, China, in 2018, and the M.Eng degree in the same major from the Shanxi Key Laboratory of Intelligent Robots, School of Mechanical Engineering, Xi'an Jiaotong University, Xi'an, China, in 2021. He is a postdoctoral researcher with the Human-Robot Interfaces and Interaction (HRII) Lab at the Italian Institute of Technology (IIT), Genova, Italy.

He was a finalist for the best paper on mobile manipulation at IROS 2022. His research focuses on robot learning, mobile manipulation, compliant control, and human-robot interaction and collaboration.

Alberto Redaelli (Fellow, EAMBES) received his PhD degree in Bioengineering in 1995 on fluid-structure interaction mechanics in the left ventricle, Politecnico di Milano, Italy. Since 2014, he has been a full professor at the Department of Bioengineering of the Politecnico di Milano. His teaching activities are in the field of Biomechanics and Computational Biomechanics. He is responsible for the Computational Biomechanics Laboratory and coordinator of the Biomechanics Research Group of the Department of Bioengineering.

He is currently a European Alliance of Medical and Biological Engineering and Science (EAMBES) Fellow and Associate Editor of APL Bioengineering. He has been the local coordinator of two STREP European Projects and one Marie Curie EST European Project in the nanobiotechnology area in FP6, one ICT project on heart pathologies in the VPH program, and one IRSES project in FP7 and he is currently the coordinator of one MSCA-ITN project and local coordinator of one RISE project in Horizon 2020.

Giancarlo Ferrigno (Senior Member, IEEE) received his MSc in Electronic Engineering in 1983 and PhD in Bioengineering in 1990 from Politecnico di Milano, Italy. After six years as a senior researcher in a private foundation, he started his academic career at Politecnico di Milano University where he is today Full Professor in the Electronic Information and Bioengineering Department (DEIB) (Assistant Professor in 1990, Associate Professor in 1998 and Full Professor in 2001).

He chaired the PhD program in Bioengineering from 2001 to 2004. From 2004 to 2006 he was appointed director of the Politecnico di Milano PhD School. From 2007 to 2009 he directed the Bioengineering Department. Since 2016 he has been chair of the Bioengineering division of the Department of Electronics, Information, and Bioengineering. In 2008 he founded the Neuroengineering and Medical Robotics Laboratory (NEARLab). He has been responsible for grants from the Italian Research Ministry, Industrial Companies, Italian Space Agency.

Elena De Momi (Senior Member, IEEE) received her MSc in Biomedical Engineering in 2002, and her PhD in Bioengineering in 2006, and she is currently a Full Professor in the Electronic Information and Bioengineering Department (DEIB) of Politecnico di Milano. She was co-founder of the Neuroengineering and Medical Robotics Laboratory, in 2008, being responsible for the Medical Robotics section (NEARLab, MRS).

She is currently the Senior Editor of the International Journal of Robotics Research, Editor of the IEEE Robotics and Automation Magazine, and Associate Editor of the IEEE Transaction on Robotics, IEEE Robotics and Automation Letters, and the IEEE Transaction on Biomedical Engineering. She has been the Publication Chair and Co-Chair for IEEE ICRA 2019, 2023, and 2024 and the Program Chair of IEEE IROS 2025.

Her research interests include Computer Vision, Soft Robots, and Human-robot Interaction in the field of medical applications.